

# TANGLED VORTEX LINES: DYNAMICS, GEOMETRY AND TOPOLOGY OF QUANTUM TURBULENCE

Carlo F. Barenghi

**Abstract** Near absolute zero, superfluid liquid helium displays quantum properties at macroscopic length scales. One property, superfluidity, means flow with zero viscosity. Another property, the existence of a complex wavefunction, constrains the rotation to thin, discrete vortex lines carrying one quantum of circulation each. Therefore, if liquid helium is stirred, it becomes turbulent, but in a peculiar way: it is a state of turbulence consisting of a tangle of quantised vortex lines in a fluid without viscosity. Surprisingly, this disordered state, which I called quantum turbulence years ago, shares many properties with ordinary turbulence as it represents its essential skeleton. These lectures attempt to relate the dynamics, the geometry and the topology of quantum turbulence. Although recently much progress has been made, there are still many open questions. Some of the methods which have been used and are described here (e.g. the smoothed vorticity, the use of crossing numbers) have a scope which clearly goes beyond the fascinating problem of turbulence near absolute zero.

## 1 Motivation: is turbulence knotted?

Images of turbulent flows display a high degree of geometrical and topological complexity: streamlines, vortex lines and magnetic field lines are apparently chaotic, twisted, perhaps linked and knotted. An example of such tangled field lines is shown in Fig.1 displaying the Earth's magnetic field in the core region. Are these field lines knotted? If so, why?

Although the governing equations of motion are well-known, the complicated geometries and topologies which are consequences of the dynamics are often sur-

---

Carlo F. Barenghi  
School of Mathematics, Statistics and Physics and Joint Quantum Centre Durham-Newcastle, Newcastle University, Newcastle-upon-Tyne, NE1 7RU, United Kingdom. e-mail: carlo.barenghi@newcastle.ac.uk

prising. The importance of turbulence in applications which range from weather forecasting to astrophysics to engineering motivates the search for a better understanding of the relation between dynamics, geometry and topology in turbulent flows. A first step in this direction is to find suitable ways to quantify the complexity of field lines which are observed or numerically computed.

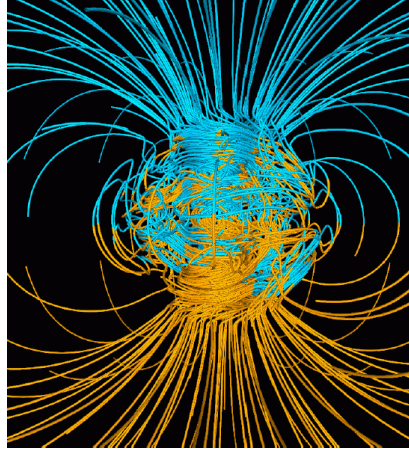


**Fig. 1** Field lines of the Earth's magnetic field. The field lines are tangled in the Earth's core region where the turbulent convection which generates the magnetic field takes place. The lines are colour-coded depending on the direction of the radial magnetic field. From Ref. [1].

The aim of these lectures, which are dedicated to an audience with a background in applied mathematics and classical physics, is to shift the context slightly, from the traditional setting of turbulent fluids which obey the Navier-Stokes equation and the equations of magneto-hydrodynamics, to the realm of turbulent *quantum fluids* where vortices are quantised. We shall see that in these more exotic systems, the quantisation of the circulation introduces a constrain which simplifies the task of measuring the complexity of turbulence, at least in principle. The price to pay is that we have to abandon the familiar world of classical physics, and consider what happens to matter at very low temperatures, a fascinating topic per se.

These lectures are organized in the following way. Section 2 contains a brief conceptual history of quantum fluids. Section 3 explains what is a quantum vortex (or vortex line) and compares it to an ordinary classical vortex. Sections 4, 5 and 6 are dedicated respectively to the geometry, the dynamics and the topology of turbulent tangles of quantum vortices. Conclusions are (not) drawn in Section 7.

## 2 A BRIEF HISTORY OF QUANTUM FLUIDS

The concept of absolute zero was probably invented by the French scientific instrument maker Guillaume Amontons (1663-1705). He measured the changes of pressure in a gas induced by changes of temperature, and argued that, since the pressure cannot become negative, there must be a minimum temperature, which he estimated at  $-240$  C (Celsius degrees). This value is not far from the modern accepted value of absolute zero, which is  $-273.15$  C, corresponding to  $0$  K (Kelvin degrees). The idea of absolute zero was consistent with the existence of atoms and the kinetic theory of gases, pioneered by the Swiss mathematician Daniel Bernoulli (1700-1782): if the temperature is the average kinetic energy of the atoms, then, if motion ceases, temperature must vanish too.

Unfortunately the popularity of the caloric theory of Antoine Lavoisier (1743-1794) halted the development of the science of cold for a number of years. Later, during the XIX century, progress restarted: thermodynamics and then statistical mechanics convinced physicists that if thermal disorder is reduced, the fundamental properties of matter become more apparent. This idea stimulated a race to achieve lower and lower temperatures. Although the race was motivated by fundamental physics, it indirectly created technologies which changed life, e.g. the refrigeration of food.

Since a gas becomes a liquid if it is cooled to a sufficiently low temperature, the liquefaction of the known gases became milestones towards absolute zero. For example, in London, Michael Faraday (1791-1867) liquefied ammonia at  $-33$  C and chlorine at  $-34$  C. In 1887, Louis-Paul Cailletet (in Paris) and Raoul-Pierre Pictet (in Geneva) liquefied oxygen at  $-187$  C. In 1877, in Krakow, Syzgunt von Wroblewsky and Karol Olszewsky liquefied nitrogen at  $-196$  C. The attention focused on the last remaining known gas to liquefy: hydrogen. In 1898, in London, James Dewar liquefied hydrogen at  $-253$  C, and thought he had won the race. However the discovery of a new element, helium ( $^4\text{He}$ ), first in the light from the Sun then in Earth's minerals, soon restarted the race. Dewar's main competitor was Heike Kamerlingh Onnes in Leiden. In 1908 Onnes liquefied helium at  $-270$  C and won the race. Soon after, in 1911, Onnes also discovered that the electrical resistance of mercury vanishes at temperatures lower than  $4.2$  K. He understood that he had found a new state of matter, which he called a *superconductor*.

In the following years, Onnes and collaborators realized that liquid helium acquires unusual thermal and mechanical properties below a critical temperature  $T_\lambda = 2.17$  K which they called the *lambda point*<sup>1</sup> For example, if helium is cooled by reducing the pressure of the vapour above the liquid surface, as soon as the temperatures  $T$  drops below  $T_\lambda$ , the liquid surprisingly stops boiling, becoming a perfect conductor of heat. Another example is that, if further cooled, liquid helium does not become solid, as all substances do. To obtain solid helium, a great pressure must be applied ( $\approx 25$  atm). Physicists called *helium II* the low temperature phase of liquid

---

<sup>1</sup> The name comes from the shape of the specific heat vs temperature curve which has a sharp spike at  $T = T_\lambda$ .

helium below the lambda point, to distinguish it from liquid helium above  $T_\lambda$  which behaves like any ordinary fluid and which they called *helium I*. Hereafter we shall be concerned only with helium II.

On the theoretical side, in the early 1900s the new science of quantum mechanics revealed that matter has wave properties, for example a particle of mass  $m$  and velocity  $v$  behaves like a wave of de Broglie wavelength  $\lambda = h/(mv)$  where  $h$  is Planck's constant. According to statistical mechanics, the average kinetic energy of a gas,  $mv^2/2$ , is proportional to  $T$ , hence  $\lambda \sim T^{-1/2}$ . The natural question arises as to what happens as  $T \rightarrow 0$ . The question is particularly relevant for a gas of bosons (particles with integer spin), which, unlike fermions (particles with half-integer spin), are not prevented by Pauli's principle from occupying the same quantum state, but can pile up into the ground state. Satyendra Bose and Albert Einstein considered an ideal gas of boson particles. They found that, at temperatures below a critical value  $T_c$ , the de Broglie wavelength becomes larger than the average distance between the particles. Essentially, the particles behave collectively like a giant wave: the entire gas is governed by a macroscopic wavefunction  $\Psi$ , creating a new state of matter which is now called a *Bose-Einstein condensate* [2, 3]. As the temperature is reduced below  $T_c$ , a larger and larger fraction of the particles condenses into the ground state; at  $T = 0$ , all particles are in the ground state.

In 1938 Peter Kapitza discovered that helium II can flow through narrow slits or thin capillaries as if it has zero viscosity. He called this property *superfluidity* (motion without viscous dissipation), in analogy to *superconductivity* (motion without ohmic dissipation). In the same year, Fritz London made for the first time the link between helium II and Bose-Einstein condensation. He also highlighted the importance of the quantum mechanical zero point energy, which, in helium II, is too large for the liquid to freeze and to become a solid at normal pressure.

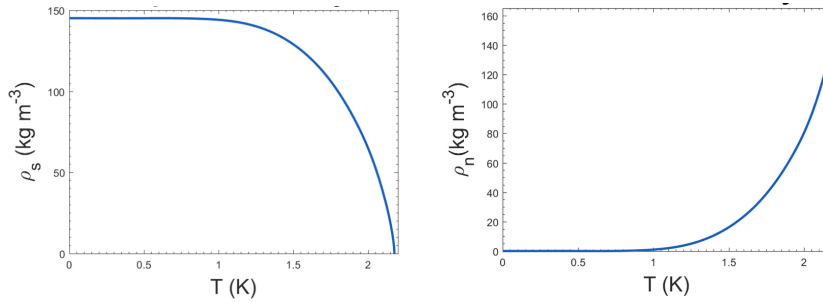


**Fig. 2** Superfluid density  $\rho_s$  (left) and normal fluid density  $\rho_n$  (right) vs temperature  $T$ .

In the 1940s Lev Landau and Laszlo Tisza developed the *two-fluid model* of helium II, describing it as the mixture of two inter-penetrating fluid components: the superfluid and the normal fluid. The model is summarized by the following table:

fluid component	density	velocity	viscosity	entropy
normal fluid	$\rho_n$	$\mathbf{v}_n$	$\eta_0$	$S_0$
superfluid	$\rho_s$	$\mathbf{v}_s$	0	0

Each fluid component has its own density and velocity fields:  $\rho_s, \mathbf{v}_s$  for the superfluid, and  $\rho_n, \mathbf{v}_n$  for the normal fluid. The superfluid has zero entropy and zero viscosity, whereas the normal fluid, consisting of thermal excitations, is viscous and carries the entire heat content of the liquid. While the total density of liquid helium,  $\rho = \rho_s + \rho_n$ , changes only a little with temperature, the superfluid and normal fluid fractions,  $\rho_s/\rho$  and  $\rho_n/\rho$ , are rapid functions of temperature: at  $T = T_\lambda$  we have  $\rho_s/\rho = 0$  and  $\rho_n/\rho = 1$ , whereas at  $T = 0$  we have  $\rho_s/\rho = 1$  and  $\rho_n/\rho = 0$ , as shown in Fig. 2. It is apparent from Fig. 2 that for  $T < 1$  K helium II is effectively a pure superfluid. Physically, the inviscid superfluid component is related to the ground state<sup>2</sup> while the normal fluid consists of thermal excitations. At small velocities, the superfluid can be modelled by the classical Euler equation for an inviscid fluid, and the normal fluid by the classical Navier-Stokes equation for a viscous fluid.

The two-fluid model explained the phenomenology of helium II (including for example the exceptional ability to transport heat, which is exploited in many applications of cryogenic engineering) and predicted new phenomena which were subsequently observed (for example, second sound, an oscillation in which superfluid and normal fluid move in antiphase, corresponding to a temperature wave at constant density and pressure).

Landau also understood that the property of superfluidity arises from the dispersion relation of the elementary excitations. Using only the laws of conservation of energy and momentum, he predicted that an object moving slower than a certain critical velocity is unable to reduce its energy by creating an excitation in the liquid, thus perceiving the surrounding liquid as a vacuum.

In 1972 Douglas Osheroff, David Lee and Robert Richardson discovered that the rare lighter isotope of helium,  $^3\text{He}$ , if cooled to temperatures of few mK, also becomes superfluid. The effect is notable because  $^3\text{He}$  is a fermion (the  $^3\text{He}$  nucleus contains two protons and only one neutron, not two), so Bose-Einstein condensation occurs via the formation of Cooper pairs like in superconductors.

In 1995, Carl Wieman, Eric Cornell and Wolfgang Ketterle cooled a very dilute weakly-interacting atomic gas to a temperature of about 100 nK; for the first time they experimentally achieved Bose-Einstein condensation in a scenario similar to the ideal gas scenario which was envisaged by Bose and Einstein.

In the following years other quantum fluids were discovered and investigated. Besides  $^4\text{He}$ ,  $^3\text{He}$  and a large number of atomic condensates (lithium, sodium, potassium, rubidium, caesium, hydrogen, etc), the realm of quantum fluids now comprises polaritons, magnons, various two-component condensates, quantum ferrofluids, spinor condensates, the interior of neutron stars and probably even dark matter axions.

---

<sup>2</sup> It must be noticed that the superfluid fraction is not the same as the condensate fraction: helium II is a liquid, and the interaction between atoms is much stronger than in a dilute gas.

Hereafter, pursuing tangled field lines, we shall focus the attention on superfluid helium (i.e. helium II, the low temperature phase of liquid  $^4\text{He}$ ), the system for which we have more experimental and theoretical information about quantum vortices and turbulence. Occasionally we shall make reference to atomic condensates because the main theoretical model of atomic condensates, the Gross-Pitaevski equation, is also used as a convenient qualitative model of helium II. For comparison, we shall also make reference to ordinary classical fluids obeying the Euler equation or the Navier-Stokes equation.

### 3 QUANTUM VORTICES

#### 3.1 Quantisation of the circulation

Helium II is remarkable not only for the absence of viscosity, but also for the quantized vorticity. This property is a consequence of the existence of a complex macroscopic wavefunction,  $\Psi$ , which rules the system. It is useful to write  $\Psi$  in terms of its magnitude and phase as

$$\Psi(\mathbf{x}, t) = |\Psi(\mathbf{x}, t)|e^{i\phi(\mathbf{x}, t)}, \quad (1)$$

where  $\mathbf{x}$  and  $t$  denote position and time respectively. Because of the phase  $\phi$ , each part of the system "knows" what happens at other parts of the system (this is how a gas of individual atoms becomes a condensate).

Using standard relations from quantum mechanics (Madelung transformation), we define number density,  $n(\mathbf{x}, t)$ , and velocity,  $\mathbf{v}(\mathbf{x}, t)$ , as

$$n(\mathbf{x}, t) = |\Psi(\mathbf{x}, t)|^2, \quad \mathbf{v} = \frac{\hbar}{m} \nabla \phi(\mathbf{x}, t), \quad (2)$$

where  $\hbar = h/(2\pi)$ . Since the curl of a gradient is always zero, Eq. 2(b) implies that the vorticity is zero. However, as we shall see, this does not mean that the circulation is necessarily zero. Consider a closed path  $C$  around a simply-connected region  $S$  (i.e. a region  $S$  such that any path  $C$  within  $S$  can be shrunk to a point which is inside  $S$ ). The circulation of the velocity around the path  $C$  is defined as

$$\Gamma = \oint_C \mathbf{v} \cdot d\mathbf{r}. \quad (3)$$

Since  $S$  is simply-connected, we can apply Stokes's Theorem, use  $\nabla \times \mathbf{v} = \mathbf{0}$ , and conclude that the circulation is zero:

$$\Gamma = \oint_C \mathbf{v} \cdot d\mathbf{r} = \int_S (\nabla \times \mathbf{v}) \cdot d\mathbf{S} = 0. \quad (4)$$

Now suppose that the region  $S$  is multiply connected, i.e. if we shrink  $C$  to a point,  $C$  may not remain within  $S$ . In other words, suppose that the region  $S$  contains a hole (a

point or a region where  $\Psi = 0$ , hence, from Eq. 2(a), the fluid's density is zero). Then Stokes's Theorem cannot be applied; using Eq. 2(b), we find that the circulation is an integer multiple of a constant  $\kappa = h/m$  called the *quantum of circulation*:

$$\Gamma = \oint_C \mathbf{v} \cdot d\mathbf{r} = \frac{\hbar}{m} \oint_C \nabla\phi \cdot d\mathbf{r} = \frac{\hbar}{m} \Delta\phi = \frac{\hbar}{m} 2\pi q = q\kappa, \quad (5)$$

where  $\Delta\phi = 2\pi q$  is the change of the phase going around the closed path  $C$ , and  $q$  is an integer (the last step follows from the fact that the wavefunction is defined up to a phase factor which is either zero or an integer multiple of  $2\pi$ ). If  $q$  is nonzero, according to Eq. 2(b), the changing phase around the hole means that there is a velocity field  $v$  around the hole: taking for  $C$  a circle of radius  $r$ , we find that the azimuthal velocity  $v$  is

$$v = \frac{q\kappa}{2\pi r}. \quad (6)$$

Eq. 6 represents the well-known velocity field around a vortex line of fluid dynamics textbooks. In most situations of interest, multi-charged quantum vortices (quantum vortices with  $q > 1$ ) are energetically unstable and decay in  $q$  singly-charged ( $q = 1$ ) quantum vortices. Therefore hereafter we assume that all quantum vortices are singly-charged ( $q = 1$ ).

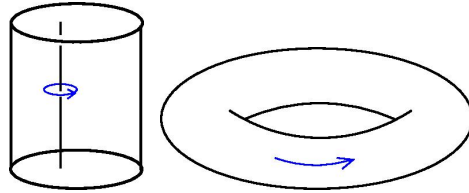


**Fig. 3** Examples of multiply-connected helium containers. The arrows indicate the direction of the flow corresponding to the changing phase around the hole. Left: a thin wire threads a cylindrical vessel from top to bottom [4, 5]. Right: a torus-shaped vessel [6].

The next question is under which conditions a region of fluid can be multiply-connected. This happens if the hole is part of the experimental apparatus, as shown in Fig. 3. At the left, the fluid is contained in a cylindrical vessel which is threaded by a thin metal wire extending from the top to the bottom [4, 5]: clearly  $\Psi = 0$  in the region occupied by the wire. At the right, the fluid is inside a superfluid gyroscope, a device shaped like a torus [6]. In both cases, any flow around the wire or along the torus will have quantised circulation.

A hole with a circulation around it can also form spontaneously in the fluid: in this case we have a *quantum vortex*, also called a *vortex line*. The process which leads to the spontaneous formation of a quantum vortex is called *vortex nucleation*. Vortex nucleation occurs if an object inside the fluid moves at speed exceeding a certain critical velocity [7], or, vice versa, if the fluid moves supercritically with respect

to the object or the boundary [8]. Vortex nucleation also occurs when the fluid is rapidly cooled across the critical temperature  $T_c$  [9], as shown in Fig. 4. Since the phase cannot simultaneously adjust to the same value everywhere, phase domains will appear separated by points (in two-dimensions) or lines (in three-dimensions) where the wavefunction vanishes. Such points or lines are quantum vortices. Since  $\Psi = 0$  implies that both the real part and the imaginary part of  $\Psi$  are zero, at these points the phase  $\phi = \tan^{-1}(\text{Im}(\Psi)/\text{Re}(\Psi))$  is not defined: this is why quantum vortices are called *phase defects*.

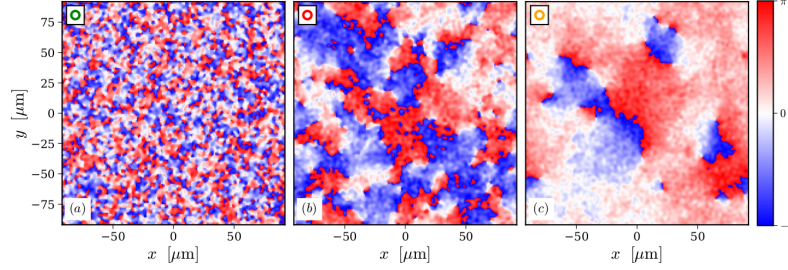


**Fig. 4** Phase distribution on the  $xy$ -plane as a gas of bosons which is suddenly cooled through the critical temperature  $T_c$ . Initially (left) the phase is random, then the interactions reduce the number of phase defects (middle) making them more visible (they are the points around which the phase changes from  $-\pi$  to  $+\pi$ ); at later stages (right) there are only few phase defects left. From Ref. [9].

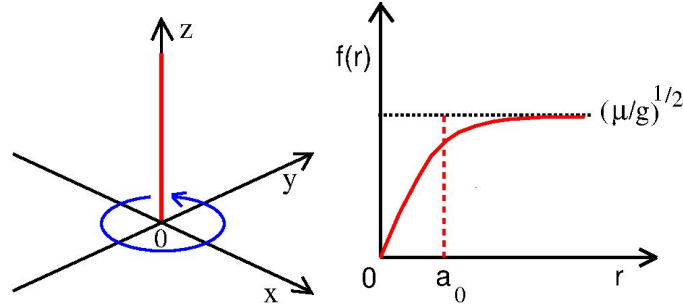


**Fig. 5** Left: vortex line aligned along the  $z$ -axis (red line: the vortex core; blue line: the superfluid velocity). Right: The solution  $f(r)$  to Eq. 11 where  $r = \sqrt{x^2 + y^2}$  is the radial distance to the vortex axis, showing that the vortex core ( $r < a_0$ ) is a region depleted of atoms. On the vortex axis the density is exactly zero.



### 3.2 The vortex core

To better understand the nature of a quantum vortex we use the Gross-Pitaevskii equation (GPE), which is a model of a weakly-interacting Bose gas at zero temperature [3] (keeping in mind that although the GPE is a good quantitative model of atomic gases, it is only a qualitative model of helium II):

$$i\hbar \frac{\partial \Psi}{\partial t} = -\frac{\hbar^2}{2m} \nabla^2 \Psi + g|\Psi|^2 \Psi - \mu \Psi. \quad (7)$$

Here  $m$  is the mass of one atom,  $g = 4\pi\hbar^2 a_s/m$  is the interaction parameter,  $a_s > 0$  is the (repulsive) scattering length between the atoms, and  $\mu$  is the chemical potential. Using Eq. 2, the GPE can be cast in the following hydrodynamical form (this is why we use the term "quantum fluid"):

$$\frac{\partial \rho}{\partial t} + \nabla \cdot (\rho \mathbf{v}) = 0, \quad (8)$$

$$\frac{\partial \mathbf{v}}{\partial t} + (\mathbf{v} \cdot \nabla) \mathbf{v} = -\frac{1}{\rho} \nabla p + \frac{\hbar^2}{2m^2} \nabla \left( \frac{\nabla^2 \sqrt{\rho}}{\sqrt{\rho}} \right), \quad (9)$$

where  $\rho = mn$  is the mass density, and the pressure is  $p = g\rho^2/(2m^2)$ . Eq. 8 is the classical continuity equation of fluid dynamics representing conservation of mass. Without the second term on the right hand side (called the *quantum pressure term*), Eq. 9 is the classical Euler equation for a compressible inviscid fluid. It can be shown that, at length scales larger than the *healing length*  $\xi = \hbar/\sqrt{gmn_0} = \hbar/\sqrt{\mu m}$ , the quantum pressure becomes negligible compared to the pressure, and we recover classical Euler dynamics. Indeed, this is what we expect in the limit as  $\hbar \rightarrow 0$ . The quantum pressure is responsible for physical effects which go beyond Euler dynamics, such as the structure of the vortex core, vortex nucleation and vortex reconnections.

The steady uniform solution of the GPE is  $\Psi_0 = \sqrt{\mu/g}$ , corresponding to the number density  $n_0 = |\Psi_0|^2 = \mu/g$ . Using cylindrical coordinates, the steady solution for a singly-charged ( $q = 1$ ) vortex placed at the origin of a uniform condensate and aligned along the  $z$ -direction as in Fig. 5(left) is

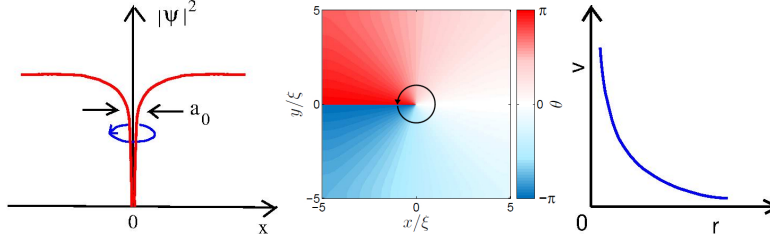
$$\Psi(r, \theta) = f(r)e^{i\theta}, \quad (10)$$

where  $f(r) = |\Psi|$  satisfies

$$-\frac{\hbar^2}{2m} \left( \frac{d^2 f}{dr^2} + \frac{1}{r} \frac{df}{dr} - \frac{f}{r^2} \right) + g f^3 - \mu f = 0. \quad (11)$$

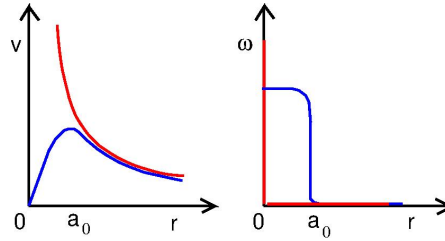
The boundary conditions are that  $f(r) \rightarrow 0$  for  $r \rightarrow 0$  and  $f(r) \rightarrow \sqrt{\mu/g}$  for  $r \rightarrow \infty$ , where  $r$  is the distance to the origin. By solving numerically Eq. 11, we find that  $f(r)$  grows from  $f = 0$  at  $r = 0$  (the axis of the vortex) to the bulk value  $\sqrt{\mu/g}$  over a characteristic distance  $a_0$  which is called the *vortex core radius*, see

Fig. 5(right). It turns out that the vortex core radius  $a_0$  is of the order of the healing length  $\xi$ .



**Fig. 6** Vortex solution of the GPE. Left: density profile  $n = |\Psi|^2$  across the vortex. Middle: phase on the  $xy$ -plane. Right: azimuthal velocity  $v = \kappa/(2\pi r)$  vs  $r$ .

Fig. 6 schematically describes the vortex solution of the GPE: a density hole surrounded by a phase which changes from 0 to  $2\pi$ , corresponding to the azimuthal velocity field  $v = \kappa/(2\pi r)$ . The fact that  $v \rightarrow \infty$  as  $r \rightarrow 0$  is not a problem: since the density  $n \rightarrow 0$  as  $r \rightarrow 0$ , there are no atoms which move at infinite speed<sup>3</sup>.



**Fig. 7** Azimuthal velocity  $v$  (left) and axial vorticity  $\omega$  (right) as a function of radius  $r$  corresponding to the quantum vortex solution of the GPE (red), and the typical Rankine profile of classical fluids (blue) which combines  $v \sim r$  for  $r < a_0$  and  $v \sim 1/r$  for  $r > a_0$ . Note that the vorticity of the quantum vortex is zero for  $r > 0$  and nominally infinite at  $r = 0$ .

It is instructive to keep track of the similarities and the differences between quantum vortices and classical vortices (described by the Euler equation or the Navier-Stokes equation). Fig. 7 compares velocity and vorticity fields of a classical vortex (blue curves) to a quantum vortex solution of the GPE (red curves). The classical vortex combines an inner region consisting of a solid-body rotating core (where the azimuthal velocity is proportional to  $r$  and the axial vorticity is constant) with an outer region which is irrotational (azimuthal velocity proportional to  $1/r$  and zero vorticity); the density can be constant at all values of  $r$ . The quantum vortex has,

<sup>3</sup> The wavefunction  $\Psi$  is well behaved on the vortex axis; what becomes singular when  $r \rightarrow 0$  is the Madelung transformation, Eq. 2.

by definition, density which vanishes at  $r = 0$ , velocity which is strictly proportional to  $1/r$  everywhere, and delta-function vorticity concentrated on the vortex axis at  $r = 0$ .

In most experiments with atomic condensates, the size of the condensate,  $D$ , is larger but not much larger than the vortex core size  $a_0$ ; typical values are  $a_0 \approx 0.1 \mu\text{m}$  and  $D$  ranging from  $D \approx 10a_0$  to  $\approx 100a_0$ ; the average inter-vortex distance,  $\ell$ , is typically  $\ell \approx 10a_0$ .

In helium II, the vortex core radius,  $a_0 \approx 10^{-10}$  m, is many orders of magnitude smaller than  $D$  and  $\ell$ , typically  $D \approx 0.1$  to  $10^{-3}$  m and  $\ell \approx 10^{-3}$  to  $10^{-5}$  m. The smallness of  $a_0$  compared to  $D$  and  $\ell$  is the reason why the Vortex Filament Model (see Section 5) is a good model of helium experiments.

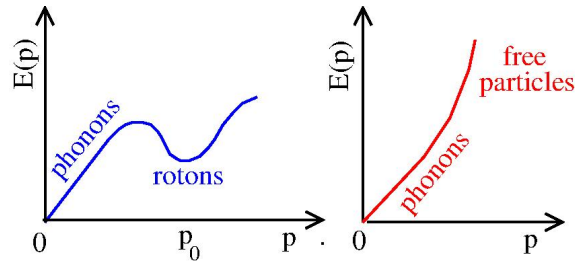


**Fig. 8** Left: dispersion relation of the elementary excitations in helium II. Energy  $E(p)$  vs momentum  $p = \hbar k$  where  $k$  is the wavenumber. Note the phonon region, where  $E \sim p$ , and the roton's minimum at  $p \approx p_0$ . Right: dispersion relation of the elementary excitations predicted by the GPE. The phonon region is followed by free particles  $E(p) \sim p^2$  without a roton minimum.

### 3.3 More insight into the vortex core

At this point it is worth exploring in more detail the nature of the vortex core in helium II beyond the simple description offered by the GPE; this information will be useful when introducing helicity. We have seen that the GPE predicts a depleted density profile with zero density on the vortex axis, as in Fig. 5 (right), and a velocity profile which diverges as  $r \rightarrow 0$ , as in Fig. 6 (right). It has already been mentioned that although the GPE is a quantitative model of atomic gases, it is only a qualitative model of helium II: helium II is a strongly-interacting liquid, not a dilute gas, and the superfluid fraction is not exactly the condensate. The dispersion relation of the elementary excitations of the uniform solution of the GPE consists of phonons at small momentum  $p$  and free particles at large  $p$ , without the roton minimum which is characteristic of liquid helium [10], see Fig. 8. Rotons require a more sophisticated many-body quantum mechanical description which reveals that the vortex structure in helium II is more complex [11, 12] than predicted by the GPE.

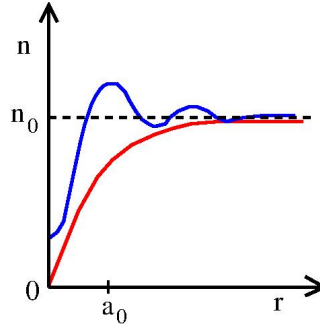


**Fig. 9** Schematic profiles of the number density  $n(r)$  vs radius  $r$  near the vortex axis at  $r = 0$ . The red line is the prediction of the GPE, the blue line is the prediction of N-body quantum mechanics. Here  $n_0$  is the bulk number density and  $a_0$  is the vortex core radius.

Consider a straight helium vortex. The N-body wavefunction  $\Psi(\mathbf{R})$ , where  $\mathbf{R} = (\mathbf{r}_1, \mathbf{r}_2, \dots, \mathbf{r}_N)$  contains the coordinates of  $N$  atoms, must be an eigenstate of the angular momentum operator with eigenvalues which are integer multiples of  $N\hbar$ . Therefore  $\Psi(\mathbf{R})$  must be complex and have the form  $\Psi(\mathbf{R}) = \Psi_0(\mathbf{R})e^{i\Omega(\mathbf{R})}$ , where  $\Omega(\mathbf{R})$  is the phase. The standard approach (called the fixed phase approximation) consists of choosing  $\Omega(\mathbf{R})$  and solving the resulting Schroedinger equation for  $\Psi_0(\mathbf{R})$  allowing interatomic correlations at short distances. The simplest choice for the phase is the Onsager-Feynman phase  $\Omega(\mathbf{R}) = \sum_{j=1}^N \theta_j$  where  $\theta_j$  is the azimuthal angle of atom  $j$  with respect to the axis of the vortex. This choice gives rise to a velocity field which is irrotational everywhere but on the vortex axis, where it diverges, making the vorticity a delta function localized on the vortex axis as in the GPE model. The equation for  $\Psi_0(\mathbf{R})$  yields a density profile  $n$  which vanishes at the vortex axis (as in the GPE model), but which also displays density oscillations near the edge of the core; these oscillations have wavenumbers typical of rotons<sup>4</sup>.

This improved vortex model can be further refined (yielding lower vortex energy, in better agreement with experiments) if the Onsager-Feynman assumption is taken only as initial guess and inter-particle correlations are taken into account also in determining the phase [14]. This refined model yields features [14, 15] which are schematically summarized in Fig. 9: the density in the core is depleted (as in the GPE model) but remains nonzero on the vortex axis, and the azimuthal velocity acquires the classical form of a Rankine vortex as in Fig. 7, with crossover from  $v \sim r$  behaviour to  $v \sim 1/r$  behaviour at length scale  $r \approx a_0$ : this second feature means that the vorticity is approximately constant inside the core.

<sup>4</sup> It is interesting to notice that the density oscillations and the roton feature of the excitations are also captured by a variant of the GPE called the Nonlocal Nonlinear Schroedinger Equation, an integral partial differential equation which replaces the hard-sphere collisions of the atoms modelled by the GPE with a smoother Lennard-Jones potential [13]).

The conclusion is surprisingly simple: according to the best microscopic information available from N-body quantum mechanics, the vortex core in helium II is similar to a classical vortex, unlike the GPE vortex structure.

## 4 GEOMETRY OF QUANTUM TURBULENCE

### 4.1 In real space

It is relatively easy to excite turbulence in a condensate. Helium II can be made turbulent by applying a heat flow (as done by W.F. Vinen, who pioneered the study of quantum turbulence), or towing a grid, or rotating propellers, or oscillating grids or forks, or applying ultrasound. Atomic condensates can be made turbulent by stirring using a laser spoon, or by oscillating or shaking the confining trap. Experimental techniques exist to detect and visualize the quantum vortices which are thus generated. Currently, the most popular visualization techniques used in helium II are based on tracer particles (typically micron-sized solid hydrogen particles which can become trapped in the vortex cores). Individual vortex lines can thus be visualized. The local velocity can be measured using a variety of local probes ranging from miniature Pitot tubes to cryogenic hot wires to mini cantilevers. Such measurements are crucial to determine the energy spectrum, that is to say the distribution of the kinetic energy over the length scales in a turbulent flow.

In atomic condensates absorption images are taken of the expanded condensate after the trap has been switched off (the expansion is necessary to make the condensate large enough to image it). Such visualization is necessarily destructive. A non-destructive stroboscopic technique also exists which can visualize a couple of vortices at the time. The main reason for which the study of quantum turbulence is more advanced in helium II than in atomic condensates is the lack of three dimensional visualization and of local velocity probes in atomic condensates.

In both helium II and atomic condensates, turbulence manifests itself as a disordered, time-dependent *tangle of vortex lines*, which move according to the velocity field which they generate and reconnect when they collide. At nonzero temperatures the vortex lines suffer a friction force when they move with respect to the normal fluid [16]; microscopically, this friction is caused by the scattering of phonons and rotons by the velocity field of the vortex lines. Turbulence thus decays in time, unless it is continually forced. Surprisingly, turbulence also decays at temperatures below 1 K where the normal fluid and the friction are negligible: in Section 5.3 we shall see that moving vortices generate sound waves (hence phonons, hence heat), thus the mechanism that destroys the kinetic energy of the vortex lines is acoustic rather than viscous.

The results of numerical simulations of turbulence are usually presented by displaying instantaneous snapshots of vortex lines, see Fig. 10. These snapshots have been generated using the Vortex Filament Model (see Section 5) using periodic

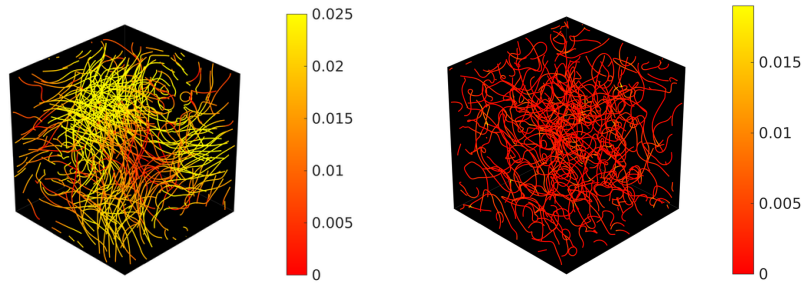


**Fig. 10** Snapshots of vortex tangles computed in a periodic cube using the Vortex Filament Model. The vortex lines are colour-coded according to the magnitude of the local helicity as explained in Section 6.3.

boundary conditions to represent a large homogeneous sample of helium II: lines which appear interrupted continue on the other side of the periodic cube.

To appreciate these images and the difference/similarities between quantum turbulence and classical turbulence it is important to notice the following. Firstly, the velocity field around each vortex line thus displayed is constrained to the irrotational form of Eq. 6 (with  $q = 1$ ) (whereas vortices in ordinary turbulence are unconstrained: they can be large and small, weak and strong); secondly, the fluid which moves around each vortex line has zero viscosity (hence will not slow down with time); thirdly, this visualization does not give information about the sense of rotation of each vortex line.

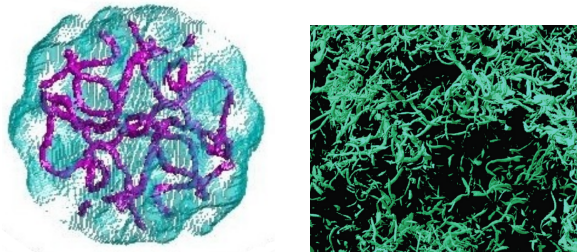


**Fig. 11** Left: Snapshots of a vortex tangle in a spherically trapped atomic condensate [17]. What is plotted is the isosurface of the density (the outer surface of the condensate in blue, the vortex cores in purple). Right: Coherent vorticity structures in ordinary turbulence. Isosurfaces of the magnitude of the vorticity, computed at an arbitrary threshold value, represent intense, localized tubular regions of high rotation. From Ref. [18].

Fig. 11 (left) shows turbulence in a spherically trapped atomic condensate. What is displayed is the density isosurface representing the wobbly, oscillating outer part of the condensate (pale blue colour), and, inside the condensate, the cores of the

vortex lines (purple colour). The quantum vortices appear as tubes, because the size of the condensate,  $D$ , is only one order of magnitude larger than  $a_0$ .

It is interesting to compare quantum turbulence with ordinary turbulence in terms of the geometry of the vorticity. As we have seen in Fig. 10 and 11 (left), quantum turbulence consists of a tangle of vortex lines constrained by the quantization of the circulation. Ordinary turbulence, computed by solving the Navier-Stokes equation, also contains tubular *coherent structures* or *vortex tubes* of intense vorticity, see Fig. 11 (right), somewhat similar to the vortex lines. Since classical vorticity is continuous, classical turbulence contains infinite vortex lines; thus these structures represent local bundles of parallel vortex lines, concentrating the vorticity enough to be recognized by the plotting algorithm. The size of the coherent structures is of the order of the Kolmogorov dissipation length scale [19]. Although the number and shape of these structures depend on the arbitrary threshold value used for plotting, the analogy is intriguing.

In helium II experiments and numerical simulations the intensity of the turbulence is usually quantified by measuring the *vortex line density*  $L$ , defined as the vortex length per unit volume. From  $L$ , one recovers the *average inter-vortex distance*,  $\ell \approx L^{-1/2}$ . There is currently no experimental technique to measure  $L$  in atomic condensates, and this is one of the reasons for which we focus on helium II here instead.

## 4.2 In $\mathbf{k}$ -space

The apparently disordered geometry of turbulence is better understood in Fourier space. Indeed, the study of turbulence of the Navier-Stokes equation focuses on the *energy spectrum*,  $\hat{E}(k)$ , which gives the distribution of the kinetic energy over the length scales  $2\pi/k$  where  $k$  is the wavenumber. The prototype problem is homogeneous isotropic turbulence, sustained in a statistical steady state by injecting energy at some large length scale  $D$  to compensate for viscous losses. A brief review of classical turbulence [19] is the following. Let  $E$  be the kinetic energy of the flow per unit mass. After Fourier transforming  $\mathbf{v}(\mathbf{r}, t)$ , the energy spectrum is defined by

$$E = \frac{1}{V} \int_V \frac{1}{2} \mathbf{v}(\mathbf{r}, t) \cdot \mathbf{v}(\mathbf{r}, t) d^3\mathbf{r} = \int_0^\infty \hat{E}(k) dk. \quad (12)$$

The energy which is injected at the scale  $D$  is shifted by the nonlinearities of the Navier-Stokes equation into smaller and smaller scales, until, at some small length scale,  $\eta$ , called the *Kolmogorov length*, viscous forces dissipate the energy into heat. This scale-by-scale transfer is called the *Richardson energy cascade*. It can be shown that the energy spectrum  $\hat{E}(k)$  satisfies the *Kolmogorov law*

$$\hat{E}(k) = C\epsilon^{2/3}k^{-5/3}, \quad (13)$$

where  $C$  is a dimensionless constant of order unity and  $\epsilon = -dE/dt$  is the rate of energy dissipation (per unit mass). It is also found that the ratio between the length scale of the energy input and the length scale of the energy dissipation is  $D/\eta \approx \text{Re}^{3/4}$  where  $\text{Re} = UD/\nu$  is the *Reynolds number*,  $U$  is the mean flow, and  $\nu$  the kinematic viscosity.

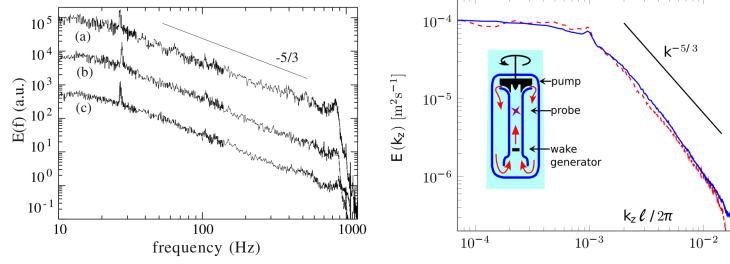


**Fig. 12** Energy spectrum measured in helium stirred by counter-rotating propellers at different temperature [20] (left) and in a superfluid wind tunnel [21] (right). In both cases, the spectrum displays a clear Kolmogorov scaling  $\hat{E}(k) \sim k^{-5/3}$ .

In helium, the Kolmogorov scaling has been observed in experiments [20, 21, 39], see for example Fig. 12. The scaling, which is considered the signature of the energy cascade, has been confirmed by numerical simulations [23, 24, 25] over the hydrodynamical range of length scales  $k_D \ll k \ll k_\ell$ , where  $k_D = 2\pi/D$  and  $k_\ell = 2\pi/\ell$ . At larger wavenumbers  $k > k_\ell$ , the spectrum has the typical  $k^{-1}$  behaviour of the spectrum of an individual vortex line, as shown in Fig. 13.

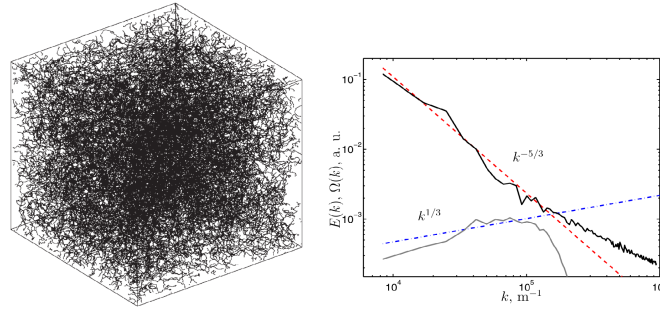


**Fig. 13** Vortex tangle computed using the VFM (left) displaying the classical Kolmogorov energy spectrum  $\hat{E}(k) \sim k^{-5/3}$  (right) for  $k < k_\ell = 1.7 \times 10^5 \text{ m}^{-1}$  which crosses over to  $\hat{E}(k) \sim k^{-1}$  for  $k > k_\ell$ . The curve below is the enstrophy spectrum with the classical scaling  $\hat{\Omega}(k) \sim k^{1/3}$  in  $k_D < k < k_\ell$ . The red and blue dashed lines are guides to the eye to represent the  $k^{-5/3}$  and the  $k^{1/3}$  scalings respectively. From Ref. [26].



To get more insight into the geometry of the turbulence, in the numerical simulations it is useful to take into account the orientation of the vortex lines by constructing the *smoothed vorticity* field,  $\omega(\mathbf{r}, t)$  [26]:

$$\omega(\mathbf{r}, t) = \kappa \sum_{j=1}^N \frac{\mathbf{s}'_j}{(2\pi\sigma^2)^{3/2}} e^{-|\mathbf{s}_j - \mathbf{r}|^2 / (2\sigma^2)} \Delta\zeta. \quad (14)$$

The notation used in this equation will be explained in Section 5.5; here it suffices to say that  $\mathbf{s}_j$  ( $j = 1, \dots, N$ ) is a discretization point along the vortex lines, and  $\mathbf{s}'_j$  is the tangent unit vector to the line at  $\mathbf{s}_j$ . Essentially, each vortex line is dressed with an oriented Gaussian function which "smooths" it over the length scale  $\sigma \approx \ell$ . Two parallel vortex lines create a strong smoothed vorticity  $\omega$ , while two antiparallel lines give a negligible  $\omega$ . From  $\omega$ , one defines the *enstrophy*  $\Omega$  and the enstrophy spectrum  $\hat{\Omega}(k)$ :

$$\Omega = \frac{1}{V} \int \omega(\mathbf{r}, t) \cdot \omega(\mathbf{r}, t) d^3\mathbf{r} = \int_0^\infty \hat{\Omega}(k) dk. \quad (15)$$

It is found [26] that the enstrophy spectrum has indeed the classical  $\hat{\Omega}(k) \sim k^{1/3}$  scaling which is expected from the  $k^{-5/3}$  Kolmogorov spectrum of the energy in the same range of  $k$ , see the bottom curve in Fig. 13.

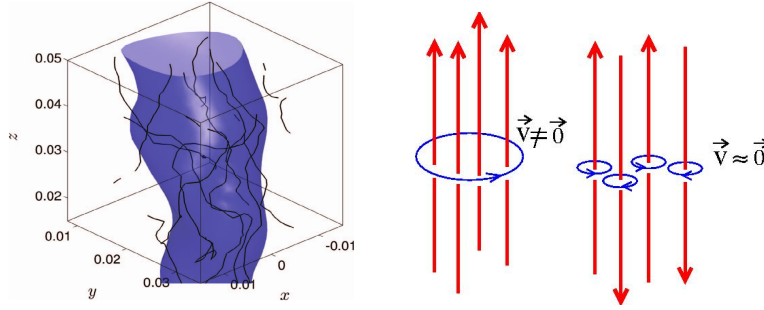


**Fig. 14** Left: magnified plot of a vortex bundle in a numerical simulation of turbulence performed using the VFM. The bundle is within the coloured region, which is an isosurface of the smoothed vorticity. Only the vortex strands which are within this region are plotted, i.e. these vortex strands are parallel. From Ref. [28]. Right: schematic bundles of vortex lines (the arrows show the direction of the vorticity). If the vortices are parallel, a large scale flow around them is created; if the orientation of the lines is random, the velocity contributions cancel out.

The conclusion [27] from these and similar experimental and numerical studies is that helium II, at length scales larger than the average inter-vortex distance  $\ell$ , behaves like a classical Navier-Stokes fluid displaying the Kolmogorov  $k^{-5/3}$  scaling (at shorter length scales, for  $k > k_\ell$ , the dynamics of individual vortex lines takes over). The question is: why?

The answer is the spontaneous partial polarisation of the vortex lines. When strong, this polarization may even take the form of visible bundles of parallel vortices. The bundles may last only a brief time before disappearing, but form again somewhere else in the flow. An example of a vortex from numerical simulations is shown in Fig. 14 (left). Within the bundle, the vortex lines are parallel, creating a relative large flow as explained in Fig. 14 (right). The bundles contain energy.

In a follow-up numerical investigation [29], a vortex tangle with energy spectrum satisfying the Kolmogorov law was analysed by instantaneously dividing the vortex lines in two groups: polarised and unpolarised (a distinction made by thresholding the smoothed vorticity), as shown in Fig. 15. It was found that, when considered separately, the polarised lines have a  $k^{-5/3}$  spectrum, while the unpolarised lines have a  $k^{-1}$  spectrum. This suggests that the Kolmogorov spectrum, which piles up energy at small  $k$ , is the effect of some partial polarization of the vortex tangle (indeed, experimental data [30] suggests that most of the energy is carried by the polarised lines). In a disordered vortex configuration, instead, the  $k^{-1}$  spectrum is a signature of randomness: it means that the velocity field at a point is dominated by the nearest vortex lines (the contribution of all other lines cancel out).

The classical behaviour of turbulent helium II at length scales  $k_D < k < k_\ell$  is confirmed by studies of the velocity statistics. The initial studies were puzzling: it was found that the normalised histograms of the velocity components display non-classical power law behaviour in the experiments [31] and in the numerical simulations [17], unlike the Gaussian behaviour observed in classical turbulence [32]. But the explanation was soon found: in the experiments the velocity components are measured using tracer particles which are smaller than the inter-vortex distance  $\ell$ , and in the simulations they are naturally computed at selected points in space. If the velocity components are averaged over length scales larger than  $\ell$  [33, 34], classical Gaussian statistics are recovered. It is therefore important to keep in mind the distinction [35] between *classical length scales* ( $k < k_\ell$ ) and *quantum length scales* ( $k > k_\ell$ ).

These results are consistent with ordinary turbulence. Farge et al. [36] used wavelets to decompose classical Navier-Stokes turbulence into a coherent part (see Fig. 16) and an incoherent part; it was found that the coherent part, consisting of "vortex tubes", is responsible for most of the energy of the flow and for the observed Kolmogorov spectrum of the entire flow.

### 4.3 Vinen turbulence

We should not rush to the conclusion that quantum turbulence is quite similar to classical turbulence, at least for  $k < k_\ell$ . A second regime of quantum turbulence has been identified, which we shall refer to as *Vinen turbulence* to distinguish it from the regime described in the previous section which we shall refer to as *Kolmogorov turbulence*. Vinen turbulence has been observed in experiments with vortex rings [38], experiments in  $^3\text{He}$  [39], numerical simulations based on the VFM [40], GPE

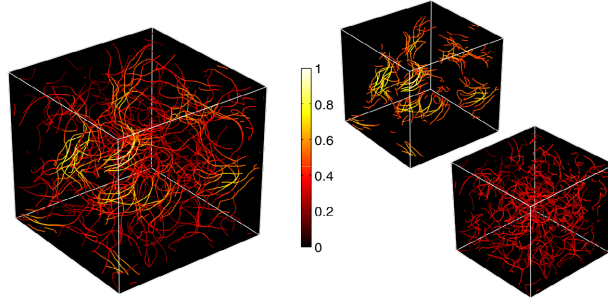


**Fig. 15** Left: snapshot of a vortex tangle computed using the VFM. The vortex lines are colour-coded according to the local smoothed vorticity (yellow regions correspond to large values, red regions to low values). On the middle and right, the same snapshot is split into locally polarised lines ( $\omega(\mathbf{s}_j, t) > 1.4 \omega_{rms}$ ) (middle) and random lines ( $\omega(\mathbf{s}_j, t) < 1.4 \omega_{rms}$ ) (right). The entire tangle (left) and the polarised lines (middle) have a  $k^{-5/3}$  energy spectrum, while the random lines (right) have a  $k^{-1}$  spectrum. From [29].

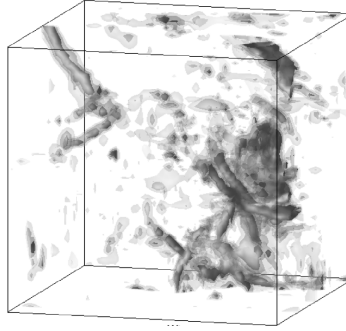


**Fig. 16** Snapshot of the coherent part of classical turbulence consisting of vortex tubes, responsible for the observed Kolmogorov  $k^{-5/3}$  energy spectrum. From [36].

simulations of the thermal quench of a Bose gas [41], GPE simulations of turbulence in an atomic condensate [42], and in simulations of dark matter [43]. The Vinen and Kolmogorov regimes can be experimentally distinguished by the rate of decay of the vortex line density, which is either  $L \sim t^{-1}$  (Kolmogorov) or  $L \sim t^{-3/2}$  (Vinen).

Vinen turbulence is different from Kolmogorov turbulence because it lacks a clear energy cascade [44]. Typically, this happens because there is no forcing at a large enough length scale, or  $k$ -space is too limited. The spectrum of Vinen turbulence thus lacks energy at the large length scales, peaks at intermediate length scales around  $k_\ell$ , and decays as  $k^{-1}$  for  $k > k_\ell$ , as shown in Fig. 17. Numerical simulations [41, 42] show that velocity correlations decay rapidly at distances larger than  $\ell$ .

It is probably correct to think of Vinen turbulence as consisting more of random vortex rings than polarised lines or bundles, as is shown schematically in Fig. 18.

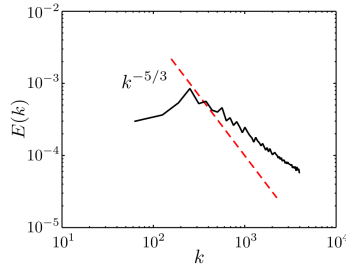


**Fig. 17** Energy spectrum of Vinen turbulence. The dashed line is a guide to the eye to indicate the Kolmogorov  $k^{-5/3}$  scaling. Notice the lack of energy at the large length scales (small  $k$ ), and the  $k^{-1}$  behaviour at large  $k$ .

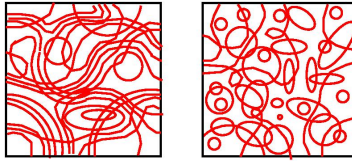


**Fig. 18** Artistic representation of vortex lines in Kolmogorov turbulence (left) and Vinen turbulence (right).

## 5 DYNAMICS OF QUANTUM TURBULENCE

The dynamics of quantum vortices in a turbulent tangle is rich in interesting effects. We have seen in Section 4 that a vortex tangle consists of a mixture of interacting vortex lines and vortex loops. It is instructive to consider the elementary physical processes which continually take place within the vortex tangle.

### 5.1 Friction

At sufficiently low temperatures the friction between the normal fluid and the vortex lines tends to zero. In this temperature regime, vortex rings of radius  $R$ , having energy proportional to  $R$ , move at translational self-induced velocity  $v_R \sim 1/R$  (the larger the radius, the slower the velocity). More in general, we shall see in Section 5.5 that, in the first approximation, curved vortex lines move in the binormal direction at velocity which is inversally proportional to the local radius of curvature. Therefore, when looking at images of vortex tangles as in Fig. 10, we should recognize that gently curved lines and large loops move slowly, while wiggly lines and small loops move rapidly. At higher temperatures, vortex lines which move with respect to the stationary normal fluid lose energy to it. For example, a vortex ring shrinks in size and speeds up, until it vanishes, as is shown in Fig. 19 (left). Similarly, the amplitude of Kelvin waves (see Section 5.2) decreases, straightening vortices.

However, the friction between the superfluid and the normal fluid can also transfer energy in the opposite direction: a moving normal fluid can feed energy into the vortex tangle. For example, if the normal fluid velocity,  $v_n$ , exceeds the self-induced velocity of the vortex ring,  $v_R$ , the ring gains energy and its radius grows [16], as is shown in Fig. 19 (right). Similarly, if the normal fluid velocity in the direction along a vortex line is large enough, infinitesimal Kelvin waves along the line become unstable and grow in amplitude (*Donnelly-Glaberson instability*).

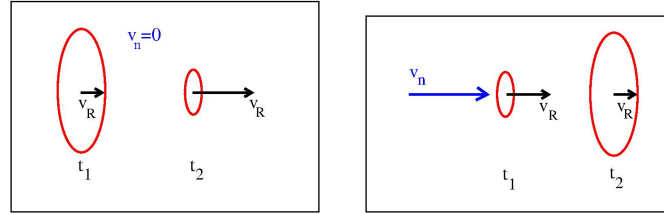


**Fig. 19** Left: schematic vortex ring shown at two successive times  $t_1 < t_2$  travelling from left to right as it decays due to friction with the stationary normal fluid ( $v_n = 0$ ). The black arrow is the ring's translational velocity  $v_R$ , which increases as the ring's radius  $R$  decreases. Right: schematic vortex ring shown at two successive times  $t_1 < t_2$  travelling from left to right as it gains energy from the normal fluid moving at velocity  $v_n > v_R$  (blue arrow) in the same direction. The black arrow is the ring's translational velocity  $v_R$ , which decreases as the radius  $R$  increases.

### 5.2 Kelvin waves

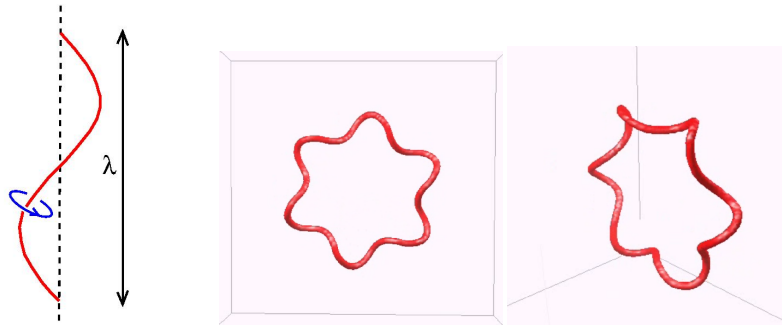


**Fig. 20** Left: schematic Kelvin wave of wavelength  $\lambda$  on a straight vortex line. The red line is the perturbed vortex core, the dashed black line is the location of the unperturbed straight vortex. Middle and right: a vortex ring, perturbed by a helical Kelvin wave having  $m = 6$  azimuthal symmetry, is shown from two different directions. Calculation performed using the GPE.

Vortex lines sustain rotating helical perturbations of their shape called *Kelvin waves*. Fig. 20 (left) shows a Kelvin wave of wavelength  $\lambda$  on a straight vortex; if the amplitude of the wave is small, the angular velocity of rotation is proportional to  $\lambda^{-2}$  (i.e. shorter waves rotate faster). Fig. 20 (middle and right) shows a vortex ring with a Kelvin wave of azimuthal symmetry  $m = 5$ . If the amplitude of Kelvin waves on a vortex ring is large, the translational velocity of the ring is reduced compared to a circular ring [45]. In general, the larger the temperature the smoother the vortex lines become, as friction damps out the Kelvin waves and cusps caused by reconnection events.

### 5.3 Sound emission

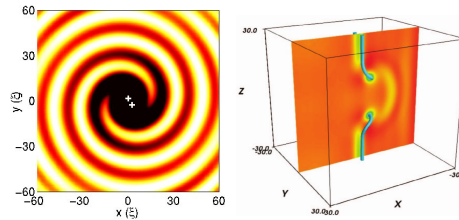


**Fig. 21** Left: Density wave pattern generated by a rotating vortex-vortex pair at the centre of the figure (marked by the two white crosses). Bright/dark colours represent density which is larger/smaller than the unperturbed density (yellow). Calculation performed using the GPE [47]. Right: Final stage of the antiparallel reconnection shown in Fig. 23: note the strong sound pulse on the plane between the two vortex lines, created at the reconnection event. Calculation performed using the GPE [50].

Kelvin waves radiate sound waves (density oscillations) as they rotate [46]. In general, when a vortex line changes its direction of motion (i.e. it accelerates), it loses energy by radiating sound waves [47], as is shown in Fig. 21 (left) for a rotating vortex-vortex pair. This mechanism of dissipation of kinetic energy is important in the case of short, rapidly rotating waves, and at low temperatures, for which friction with the normal fluid is negligible: it explains the observed decay of turbulence at temperatures as low as few mK [48]. Similarly, vortex reconnections (see Section 5.4) create a sound wave [49, 50], as is shown in Fig. 21 (right), contributing to the energy dissipation.

### 5.4 Reconnections

When vortex lines collide, they reconnect [51], as is shown schematically in Fig. 22. The reconnection of two antiparallel vortex lines computed using the GPE is shown

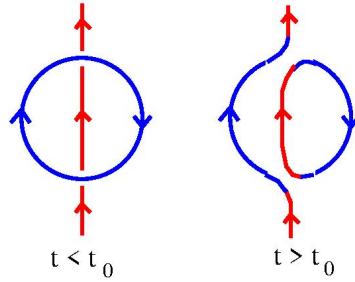


**Fig. 22** Schematic collision between a vortex ring (travelling into the page) and a stationary straight vortex line, as is also shown in Fig. 24. The arrows denote the direction of the vorticity. The figure shows that, after the reconnection at time  $t = t_0$ , part of the vortex ring has become part of the vortex line and vice versa.

in Fig. 23. Individual vortex reconnections have been experimentally observed both in helium II and in atomic condensates. Reconnections change the topology of the vortex configurations; they are physically significant because part of the kinetic energy of the colliding vortices is turned into a sound pulse [49]. Some of the initial energy is also used to create Kelvin waves, as is shown in Fig. 24: here a vortex ring travels from left to right towards a straight vortex line, and collides with it, causing two reconnection events. It is apparent from the figure that, after the collision, the vortex ring has acquired an  $m = 2$  Kelvin wave; the vortex line exhibits Kelvin waves too. Fig. 22 represents the collision schematically. If two vortex rings of the same size collide head-on, we have an *annihilation*, and the entire kinetic energy of the two vortices is turned into sound [49].

## 5.5 The Vortex Filament Model

There is not a single model which describes the phenomenology of turbulent vortices in superfluid helium. The range of physics which is accessible in helium II in the same experiment is extreme. For example, at high temperatures near  $T_\lambda$  the mean free path of thermal excitations is smaller than the vortex core, but at low temperatures it is larger than the size of the typical apparatus [52]. In ordinary fluids, these two limits are described by different models, the Navier-Stokes equation and the Boltzmann equation respectively.

There are two main models which have been used to study quantum turbulence: the GPE and the Vortex Filament Model (VFM). The advantage of the GPE is that it accounts for sound waves, vortex nucleation and vortex reconnections. The disadvantage is that it does not include the normal fluid and friction, which are well accounted by the VFM. However the VFM does not include waves and vortex reconnections (which must be performed algorithmically); moreover, the VFM does

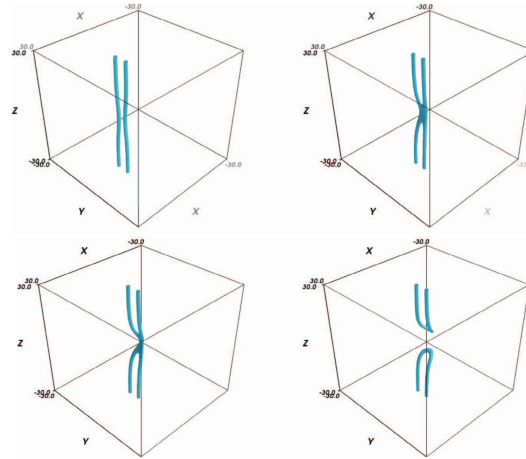


**Fig. 23** Reconnections of two antiparallel vortex lines computed using the GPE [50]. Initially ( $t < t_0$ , top left) the vortices are slightly curved in order to induce a motion which will result in a reconnection at  $t = t_0$  (top right) when the vortex cores merge; the two bottom figures show the reconnected vortex lines which move away from each other.

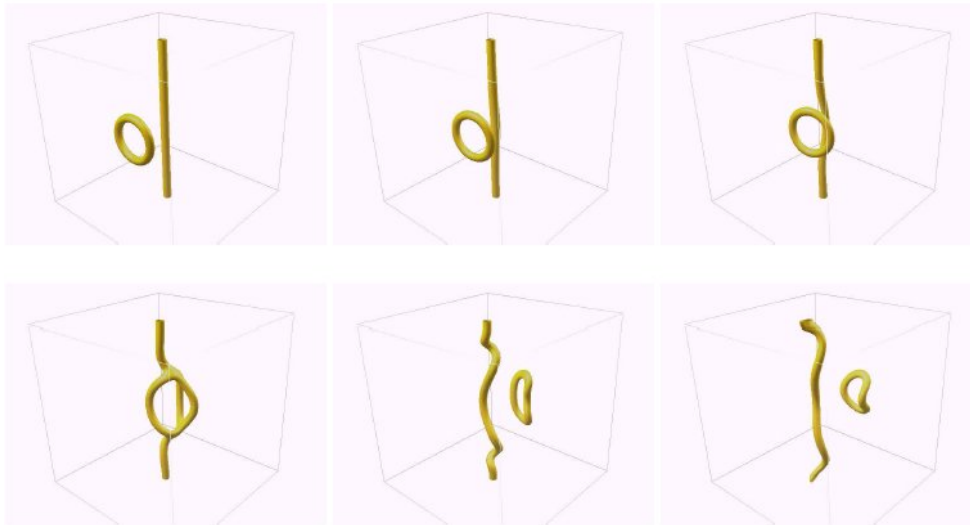


**Fig. 24** Collision of a small vortex ring travelling from left to right towards a straight vortex line computed using the condensate model. The same collision is represented schematically in Fig. 22. Density isosurfaces visualize the vortex cores. Note that after the collision the vortex ring has developed an  $m = 2$  Kelvin wave; the vortex line has Kelvin waves too. Calculation performed using the GPE.



not include nucleation, so the initial condition typically consists of some seeding vortices which can lengthen and propagate during the evolution.

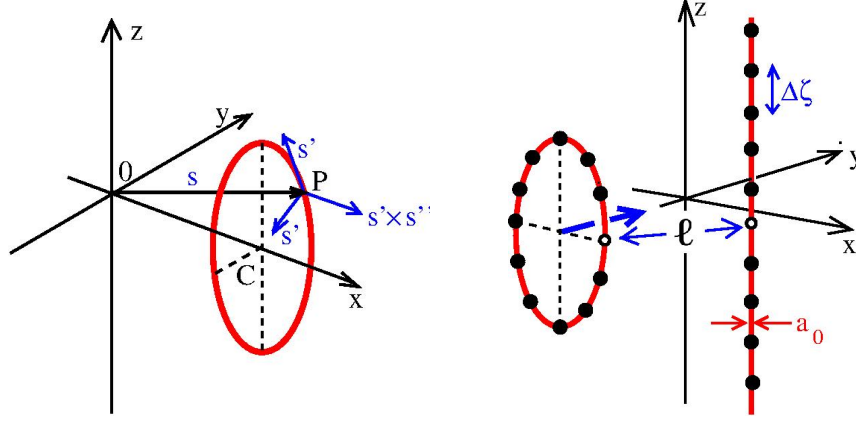


**Fig. 25** The Vortex Filament Method. Left: Vortex ring (red line) travelling in the  $x$ -direction. The plane of the ring is parallel to the  $yz$ -plane and its centre is the point  $C$ . At a point  $\mathbf{s} = \mathbf{OP}$  along the ring, the three vectors  $\mathbf{s}'$ ,  $\mathbf{s}''$  and  $\mathbf{s}' \times \mathbf{s}''$  are displayed as blue arrows. Right: a vortex ring (whose plane is parallel to the  $xz$ -plane) travels in the  $y$ -direction approaching a straight vortex line parallel to the  $z$ -axis. The discretization points along the ring and the line are marked by black circles. The figure also shows the discretization distance,  $\Delta\zeta$ , between the discretization points, the vortex core radius,  $a_0$ , and the minimum distance between the ring and the line,  $\ell$  (the discretization points used to define  $\ell$  are marked as white circles).

The VFM is built on the fact that in helium II the vortex core radius,  $a_0 \approx 10^{-10}$  m, is many orders of magnitude smaller than any length scale of the flow. The VFM describes vortex lines as space curves of infinitesimal thickness which are represented parametrically as  $\mathbf{s} = \mathbf{s}(\zeta, t)$  where  $\zeta$  is the arc length. At each point  $\mathbf{s}$  along a vortex, three orthogonal vectors are defined in the tangent, normal and binormal directions respectively:  $\mathbf{s}' = d\mathbf{s}/d\zeta$ ,  $\mathbf{s}'' = d^2\mathbf{s}/d\zeta^2$  and  $\mathbf{s}' \times \mathbf{s}''$  (where a prime denotes the derivative with respect to arc length), as is shown for a vortex ring in Fig. 25.

Consider a vortex tangle  $\mathcal{T}$  consisting of many such space curves. The space curves are discretized by a large number of points separated by the distance  $\Delta\zeta$ , representing the numerical resolution of the calculation. The discretization distance must be much larger than the expected average separation between the vortex lines,  $\ell \approx 10^{-3}$  to  $10^{-5}$  m in typical experiments. Clearly it would be computationally impossible to reduce  $\Delta\zeta$  to the dimensions of  $a_0$ , so all phenomena taking place at length scales between  $\Delta\zeta$  and  $a_0$  must be ignored.

It can be shown that, in the absence of any superfluid potential flow which is imposed externally, the point  $\mathbf{s}$  along a vortex line moves with velocity [53]

$$\frac{d\mathbf{s}}{dt} = \mathbf{v}_s + \alpha \mathbf{s}' \times (\mathbf{v}_n - \mathbf{v}_s) - \alpha' \mathbf{s}' \times (\mathbf{s}' \times (\mathbf{v}_n - \mathbf{v}_s)), \quad (16)$$

(*Schwarz's equation*) where  $\mathbf{v}_n$  is any normal fluid velocity which is imposed externally and  $\alpha, \alpha'$  are temperature-dependent friction coefficients. The superfluid velocity  $\mathbf{v}_s$  at the point  $\mathbf{s}$  is decomposed as

$$\mathbf{v}_s(\mathbf{s}, t) = \mathbf{v}_{loc}(\mathbf{s}, t) + \mathbf{v}_{non}(\mathbf{s}, t), \quad (17)$$

where  $\mathbf{v}_{loc}(\mathbf{s}, t)$  arises from the local curvature at the point  $\mathbf{s}$

$$\mathbf{v}_{loc}(\mathbf{s}, t) = \frac{\kappa}{4\pi} \ln\left(\frac{R}{a_0}\right) \mathbf{s}' \times \mathbf{s}'', \quad (18)$$

and  $\mathbf{v}_{non}(\mathbf{s}, t)$  accounts for non-local velocity contributions due to (i) other parts of the same vortex line and (ii) other vortex lines in  $\mathcal{T}$

$$\mathbf{v}_{non}(\mathbf{s}, t) = -\frac{\kappa}{4\pi} \oint_{\mathcal{T}'} \frac{(\mathbf{s} - \mathbf{s}_0(\zeta))}{|\mathbf{s} - \mathbf{s}_0(\zeta)|^3} \times \mathbf{s}'_0(\zeta) d\zeta, \quad (19)$$

(*Biot-Savart law*) where  $\mathcal{T}'$  is the vortex tangle  $\mathcal{T}$  excluding the close neighborhood of the point  $\mathbf{s}$ , thus preventing the integral from diverging. Notice that the local contribution,  $\mathbf{v}_{loc}(\mathbf{s}, t)$ , points in the binormal direction and is inversally proportional to the radius of curvature of the vortex line at  $\mathbf{s}$ , defined as  $R = 1/|\mathbf{s}''|$ . Vortex reconnections are implemented algorithmically when two vortex strands become closer than the minimum distance  $\Delta\zeta$ .

The friction coefficients  $\alpha$  and  $\alpha'$  tend to zero for  $T \rightarrow 0$ . In this limit of zero temperature, Schwarz's equation reduces to

$$\frac{d\mathbf{s}}{dt} = \mathbf{v}_s = \mathbf{v}_{loc} + \mathbf{v}_{non}, \quad (20)$$

which restates the classical Helmholtz's theorem that vortex lines move with the (super)flow.

## 6 TOPOLOGY OF QUANTUM TURBULENCE

Individual *vortex knots* and their stability have been studied for some time [54, 55, 56, 57]. Images such as Fig. 10 raise the question: are vortex lines in quantum turbulence knotted? If they are, what is the amount of this "knottiness"? If the turbulence is sustained in a statistical steady-state, does the knottiness fluctuate about a well-defined average value? Is this average value related to the intensity of the turbulence, e.g. the Reynolds number? Vortex knots can be created (and destroyed) only by reconnections, events which are associated with dissipation of kinetic energy. Therefore, a knotted vortex tangle which decays must release a certain amount of energy in the form of sound waves simply by reducing its topological complexity. Another question is whether this decay takes place along preferred topological pathways, as has been suggested [58, 59, 60]. These questions have acquired more

interest since Irvine and collaborators showed how to create vortex knots in the laboratory in a controlled, reproducible way [61].

## 6.1 Steady turbulence in open domain

The first step towards answering these questions is to quantify the knottiness of vortex tangles in ways that can be computationally implemented, ideally even in extremely dense vortex tangles such as Fig. 13. All calculations presented here refer to vortex tangles which evolve in an infinite computational domain. This is because periodic boundary conditions (used to study homogeneous isotropic turbulence) would complicate the definitions of the measures of complexity, which would not be helpful at this early stage of investigation.

Clearly it would be preferable to study regimes in which the turbulence is in a statistical steady state, so that the average properties of the turbulence can be related to how the turbulence is driven. At nonzero temperature, a statistical steady state requires a continuous input of energy by the driving normal fluid, which in an experiment would be imposed externally. The results which are presented here refer to two choices for the driving normal fluid velocity  $\mathbf{v}_n$ . The first choice consists of random waves [62] (exponentially localized in a spherical region at the centre of the computational domain). The second choice [63] is a Dudley-James flow. This flow (used in numerical models of planetary dynamos) is both solenoidal and localized in a sphere of radius  $D$ ; it has the form

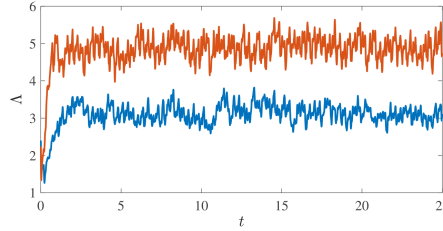


**Fig. 26** Total vortex length,  $\Lambda$ , vs time,  $t$ , for two different driving normal fluid velocities  $\mathbf{v}_n$ . The calculation starts with some seeding vortex lines. After an initial transient, the total vortex length  $\Lambda$  saturates to an average value which does not depend on the initial condition (the larger  $\mathbf{v}_n$ , the larger  $\Lambda$ ). From Ref. [63].

$$\mathbf{v}_n(r, \theta, \phi) = \sum_{l,m} (\mathbf{t}_l^m + \mathbf{s}_l^m), \quad (21)$$

where  $r, \theta, \phi$  are spherical coordinates,

$$\mathbf{t}_l^m = \nabla \times \hat{\mathbf{r}} r_l^m Y_l^m(\theta, \phi), \quad \mathbf{s}_l^m = \nabla \times \nabla \times \hat{\mathbf{r}} s_l^m Y_l^m(\theta, \phi), \quad -l \leq m \leq l, \quad (22)$$

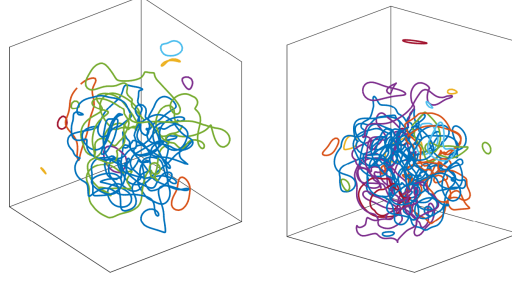


**Fig. 27** Snapshots of vortex tangles in the saturated statistic steady-state regime corresponding to the two driving normal fluid velocities of Fig. 26. Each vortex loop is colour-coded differently. From Ref. [63].

and  $Y_l^m$  are spherical harmonics. Results presented here refer to  $m = 0$ ,  $l = 2$ ,  $t_2^0 = s_2^0 = r^2 \sin(\pi r/D)$  [63].

The results obtained with these choices of  $\mathbf{v}_n$  are qualitatively similar. By forcing the turbulence in the central region only, a balance is achieved in this region between forcing and friction. The occasional vortex loop which drifts out of the central region and moves into quiescent normal fluid decays. A statistically steady-state of turbulence consisting of loops is thus created: hereafter we use the symbol  $\mathcal{T} = \bigcup_{i=1}^N \mathcal{L}_i$  to mean that the vortex tangle  $\mathcal{T}$  consists of a collection of  $N$  closed vortex loops  $\mathcal{L}_j$  ( $j = 1, \dots, N$ ); the number  $N$  fluctuates around a mean value because of continual vortex reconnections.

Fig. 26 confirms that after an initial transient, the total length of vortex lines,  $\Lambda$ , achieves well-defined average value in the statistical steady state regime. Fig. 27 shows two snapshots of vortex tangles corresponding to the small and large values of  $\mathbf{v}_n$  of Fig. 26. The energy of the vortex tangle, defined as

$$E = \frac{1}{2} \rho_s \int \mathbf{v}(\mathbf{r}) \cdot \mathbf{v}(\mathbf{r}) d^3\mathbf{r} = \rho_s \kappa \oint_{\mathcal{T}} \mathbf{v}_s \cdot \mathbf{r} \times \mathbf{s}' d\zeta, \quad (23)$$

has the same time behaviour of  $\Lambda$  shown in Fig. 26, fluctuating about a well-defined average value after the initial transient.

## 6.2 Quantifying the complexity of the turbulence

A possible strategy [64] is to operate with *crossing numbers*, as is illustrated in Fig. 28: consider a trefoil vortex loop (left), a three-dimensional, closed space curve oriented by the direction of the vorticity (indicated by arrows). We project the curve onto an arbitrary two-dimensional plane (middle) and assign the crossing number  $\epsilon = \pm 1$  to each apparent intersection in a standard way (explained in the figure caption). Interesting geometrical and topological properties can be assembled from

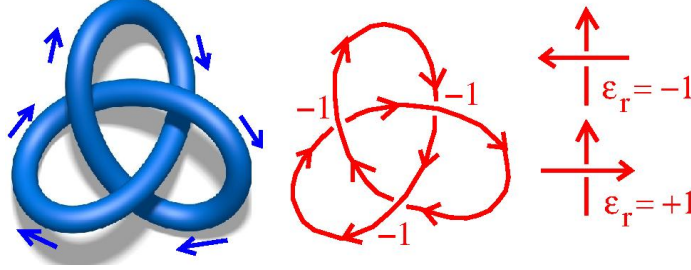


**Fig. 28** Left: a vortex in the shape of a trefoil knot; the tube represents the region of depleted density around the axis of the vortex. The axis of the tube is a three-dimensional space curve whose orientation is provided by the direction of the vorticity, that is, by the clockwise or anticlockwise direction of motion of the fluid around the vortex axis. Middle: The three-dimensional space curve is projected onto an arbitrary plane, making visible three apparent intersections; the two-dimensional curve in the figure is interrupted, to retain the information about which strand is above and which strand is below in the actual three-dimensional configuration on the left. Right: we follow the two-dimensional curve starting from an arbitrary point. At each apparent intersection,  $r$ , if the other vortex strand is above, we define a crossing number  $\epsilon_r = \pm 1$  depending on the other strand pointing right or left (if the other strand is below, we ignore this intersection and move to the next). In this example we find  $\epsilon_r = -1$  for all  $r = 1, 2, 3$ , hence obtain the writhing number  $\text{Wr} = -3$ .

these crossing numbers. For a single loop  $\mathcal{L}_i$ , the *writhing number*,  $\text{Wr}(\mathcal{L}_i)$ , provides a geometrical measure of the coiling. The definition is

$$\text{Wr}(\mathcal{L}_i) = \left\langle \sum_{r \in \mathcal{L}_i \cap \mathcal{L}_i} \epsilon_r \right\rangle, \quad (24)$$

where  $\langle \dots \rangle$  denotes averaging over all directions of projection. A measure of the total coiling of the entire vortex tangle is therefore

$$\text{Wr}(\mathcal{T}) = \left\langle \sum_{r \in \mathcal{T}} \epsilon_r \right\rangle. \quad (25)$$

In practice, numerical experiments [64] have shown that, provided the vortex tangle is sufficiently dense and isotropic, averaging over all projections is well approximated by the simpler average over the three Cartesian directions.

Another measure of the complexity of a vortex tangle is the *average crossing number*, representing the average number of apparent unsigned crossings. For two loops  $\mathcal{L}_i$  and  $\mathcal{L}_j$ , this quantity is defined as

$$C(\mathcal{L}_i, \mathcal{L}_j) = \left\langle \sum_{r \in \mathcal{L}_i \cap \mathcal{L}_j} |\epsilon_r| \right\rangle. \quad (26)$$

The generalization to the entire vortex tangle is

$$C(\mathcal{T}) = \sum_{\mathcal{L}_i, \mathcal{L}_j \in \mathcal{T}} C(\mathcal{L}_i, \mathcal{L}_j). \quad (27)$$

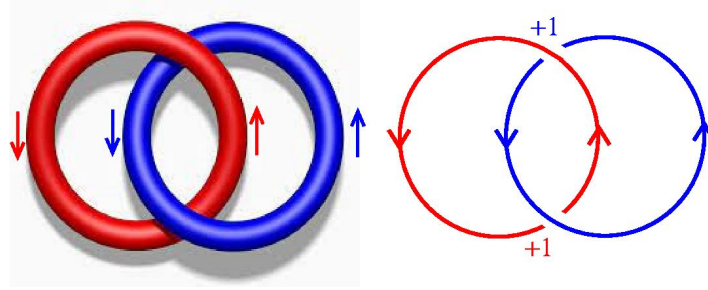


**Fig. 29** Left: Hopf link. Right: by applying Eq. 28 we find that the linking number of this vortex configuration is  $\text{Lk}(\mathcal{L}_1, \mathcal{L}_2) = (1/2)(1 + 1) = 1$ .

The linking number between two loops  $\mathcal{L}_i$  and  $\mathcal{L}_j$  is one of the most important topological invariants (it does not change if the loops are deformed). It is defined in terms of crossing numbers by

$$\text{Lk}(\mathcal{L}_i, \mathcal{L}_j) = \frac{1}{2} \sum_{r \in \mathcal{L}_i \cap \mathcal{L}_j} \epsilon_r. \quad (28)$$

An example of the calculation of the linking number is shown in Fig. 29, which shows the simplest linked structure: the *Hopf link* between two vortex loops. Notice that the linking number does not depend on the single projection over which it is calculated. Using Eq. 28, the total linking number of the entire vortex tangle is naturally defined as

$$\text{Lk}(\mathcal{T}) = \sum_{\mathcal{L}_i, \mathcal{L}_j \in \mathcal{T}, i \neq j} |\text{Lk}(\mathcal{L}_i, \mathcal{L}_j)|, \quad (29)$$

(note that contributions from self-linking are excluded). This quantity provides a simple global measure of the topological complexity of a turbulent system which can be computed relatively easy, being the vorticity discrete. It is important to notice that writhing number, average crossing number and linking number can also be calculated by performing Gauss integrals; however, it was found by numerical experiments [64] that, particularly for the dense tangles of vortices which interest us, the expressions in terms of crossing numbers are numerically more robust. The reason is that the calculation involves only integers, unlike the Gauss integrals which depend on the discretization along the space curves.

Numerical experiments confirm that the total linking number achieves a statistical steady state [62] after an initial transient, like the total length and the energy, see Fig. 30. The fluctuations, caused by reconnections which continually split and merge vortex loops, are relatively large for small vortex tangles, as expected.

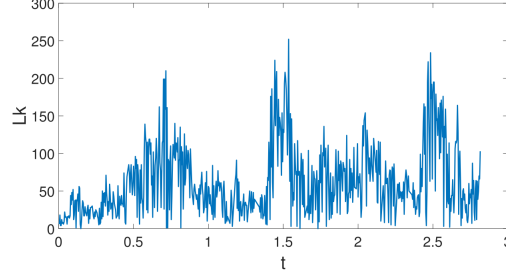


**Fig. 30** Total linking number  $Lk$  vs time  $t$  of a vortex tangle similar to Fig. 26. From Ref. [62].

### 6.3 Helicity

Another quantity which can be interpreted as a measure of the complexity of a turbulent flow is the *helicity* [65], a constant of motion under Euler evolution. In a classical flow  $\mathbf{v}$  (solution of the Euler or Navier-Stokes equation), the definition of helicity is

$$\mathcal{H} = \int_V \boldsymbol{\omega}(\mathbf{r}, t) \cdot \mathbf{v}(\mathbf{r}, t) d^3\mathbf{r}, \quad (30)$$

where  $\boldsymbol{\omega}(\mathbf{r}) = \nabla \times \mathbf{v}(\mathbf{r})$  is the vorticity. Unfortunately there is no consensus on what should be the definition of helicity for a superfluid. This problem is mainly debated in the context of the GPE, for which vorticity is a delta function centred on the vortex axis, where the azimuthal velocity diverges. A definition of superfluid helicity based on Eq. 30 thus requires [66] a careful limit for  $r \rightarrow 0$  (near the vortex axis) and opens the question whether  $\mathcal{H}$  is conserved or not under GPE evolution.

A second approach to superfluid helicity has been proposed based on the decomposition [67] of  $\mathcal{H}$  for thin vortex tubes into writhe, link and twist, in which case superfluid helicity is zero at all times [68, 69, 70]. However a subtle aspect arises: the twist has an intrinsic component which requires the construction of a second line along the vortex axis in order to define a ribbon; this is not a problem for a classical thin-cored vortex (however small the core is, it contains infinite vortex lines), but runs into the difficulty that, in the GPE model of the vortex core, there is only *one* vortex line.

A third proposal starts from the observation that the GPE only provides a simplified model of the vortex core in helium II. A better model based on N-body quantum mechanics, as explained in Section 3.3, predicts that in the core region the density does not vanish and the vorticity is uniform, thus the classical definition of helicity, Eq. 30, can be directly applied. At the mesoscale level of description provided by the VFM (which neglects physics at scales between  $a_0$  and  $\Delta\zeta$ ), using Eq. 17, one finds [71]

$$\mathcal{H} = \kappa \oint_{\mathcal{T}} \mathbf{v}_{non}(\mathbf{s}) \cdot \mathbf{s}' d\zeta = \kappa \Lambda \langle \mathbf{s}' \cdot \mathbf{v}_{non} \rangle, \quad (31)$$

where  $\langle \dots \rangle$  denotes the average over all vortex lines. Thus  $\mathcal{H}$  measures the nonlocal contribution to the lines' velocities. This result is interesting because, as mentioned in Section 5, two limiting cases of quantum turbulence characterized by different energy spectra and decay laws have been observed: Vinen turbulence and Kolmogorov turbulence. In Vinen turbulence the vortex lines are randomly oriented, which means that nonlocal contributions to the velocity of a line at a point tend to cancel out and  $\mathcal{H} \approx 0$ . In Kolmogorov turbulence, the partially polarized bundles which contain most of the energy and create the classical Kolmogorov spectrum give the necessary nonlocal velocity contributions which keeps  $\mathcal{H}$  fluctuating around a nonzero value. This interpretation of helicity is illustrated in Fig. 10: the left and right tangles (corresponding to large and small values of  $\mathcal{H}$  respectively) are examples of Kolmogorov and Vinen turbulence respectively.

## 6.4 Knottiness

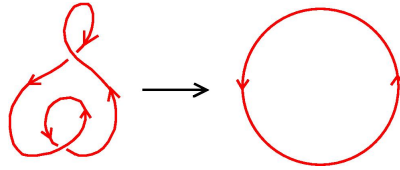


**Fig. 31** This vortex loop is an unknot: it can be deformed into a vortex ring without any reconnection. The arrows indicate the direction of the vorticity.

We have already seen that vortex tangles contain links. Now we come to the question which motivates these investigations: are the vortex lines knotted in turbulent flows? To find the answer we need to take a three-dimensional snapshot of the turbulence at a given time, consider each vortex loop  $\mathcal{L}_j \in \mathcal{T}$  at the time, and numerically determine the knot type. The last step uses [63] the association between knot types and Alexander polynomials, written in the form

$$\Delta(\tau) = c_0 + c_1\tau + c_2\tau^2 + \dots + c_\nu\tau^\nu, \quad (32)$$

where  $\nu$  is the degree of the polynomial, and  $c_0, \dots, c_\nu$  are integer coefficients (in principle, other knot polynomials could be used). For example, a vortex ring has Alexander polynomial  $\Delta(\tau) = 1$  which identifies the *unknot*: any closed vortex loop which can be deformed into a ring without reconnections (see Fig. 31) corresponds to  $\Delta(\tau) = 1$ . The simplest non-trivial knot is the *trefoil knot*, which has Alexander polynomial  $\Delta(\tau) = 1 - \tau + \tau^2$  of degree  $\nu = 2$ . In general, the larger the degree  $\nu$ , the more complex the knot type. Any vortex loop with degree  $\nu > 0$  is thus knotted (but the converse is not true, counterexamples are known). The numerical algorithm to compute the Alexander polynomials is based on finding crossings onto



projections [72] and is tested against all the knots of the Rolfsen table. Numerical checks are applied by changing the discretization along the vortex lines and by rotating the vortex loops, which changes the number of crossings. In this way, one finds the degree  $\nu_j$  of all vortex loops  $\mathcal{L}_j$  ( $j = 1, \dots, N$ ) for a given snapshot of the turbulence, where the number of loops,  $N$ , changes with time, as reconnections continually change, create and destroy knots. Data are collected over time in the statistical steady-state regime of turbulence and analyzed.

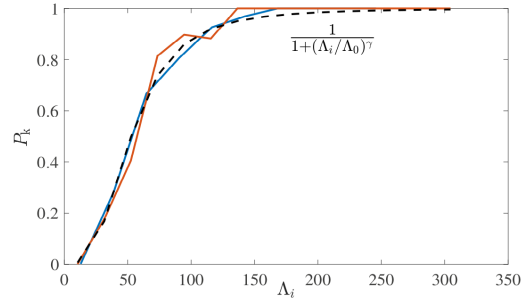


**Fig. 32** Probability  $P(\Lambda)$  that a vortex loop of length  $\Lambda$  is knotted when computed in the statistical steady state regime. From Ref. [63].

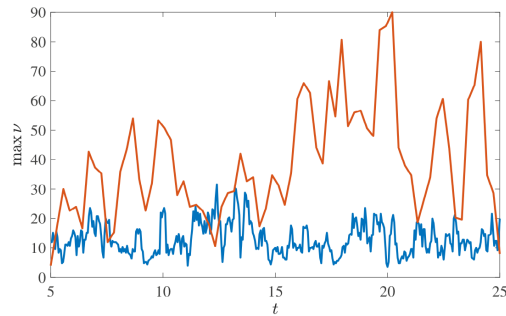


**Fig. 33** The largest (red) and the second largest (blue) degree of Alexander polynomial vs time  $t$  in the statistical state state regime. From Ref. [63].

It is found [63] that the probability  $P(\Lambda)$  that a vortex loop is knotted tends to unity if the loop is sufficiently long, see Fig. 32. This result is consistent with Monte Carlo simulations of random knotting of DNA molecules in confined volumes [73], and with experiments in which strings of different lengths were tumbled inside a box [74] (although in this case  $P(\Lambda)$  does not tend to unity at large  $\Lambda$ , perhaps due to the stiffness of the strings).

What is remarkable is that, at all times, the vortex tangles contains some vortex loops with very large degree of Alexander polynomial. Fig. 33 shows the two largest

degrees as a function of time in the statistical steady state regime: even for the small vortex tangles investigated, degrees from  $\nu = 40$  to 90 are not uncommon, and the second largest degree is typically around  $\nu = 10$  [63]. A similar result is if found if the turbulence is driven by random waves [62]. Averaged over a time window in the statistical steady state, the probability that the largest degree of Alexander polynomial is  $\nu$  appears to scale as  $\nu^{-1.5}$ .

## 7 Conclusions

At this point we can give a tentative answer to the question raised in Section 1. We have seen that quantum turbulence is, in some sense, the skeleton of classical turbulence: thin (microscopic) filaments carrying one quantum of circulation each moving in an ideal fluid background. We have seen that if we average their properties over a sufficiently large length scale, the main (macroscopic) properties of classical turbulence emerge. We have found that this turbulence is not only linked and knotted, but it contains very high degree vortex knots. Monsters are lurking in the vortex tangles.

The other main conclusion for the audience of these lectures is that, if the temperature is reduced to almost absolute zero, matter does not necessarily become a dull frozen solid, but can flow in extraordinary ways as a quantum fluid: effects of quantum mechanics appear at the macroscopic level.

The computational tools which I have presented to quantify the disorder of vortex lines have helped to distinguish the two observed regimes of quantum turbulence: Kolmogorov turbulence and Vinen turbulence. Some of the tools are not standard, for example smoothed vorticity, or the computational use of crossing numbers in dense configurations of field lines. Some tools, for example the use of knot polynomials, need to be applied more systematically to a much wider range of systems to make useful comparisons and learn which is the most useful.

The most urgent exploration would be to check if some of the tools presented here can be applied to classical turbulence, perhaps only in a statistical sense, since in a classical fluid vortex lines may not be traceable as robustly as in a quantum fluid.

**Acknowledgements** I am grateful to collaborators who taught me many things, particularly David Samuels, Andrew Baggaley, Luca Galantucci and Ladik Skrbek. The work of Mae Mesgarnezhad and Rob Cooper was essential for Section 6. Above all, I am indebted to Renzo Ricca, whose enthusiasm and focus on what is important triggered and sustained my interest in topological fluid dynamics. The support of UKRI is acknowledged.

## References

1. Glatzmaier, G.A., and Roberts, P.H.: A three-dimensional self-consistent computer simulation of a geomagnetic field reversal. *Nature*, **377**, 203 (1995).
2. Pitevskii, L., and Stringari, S.: *Bose-Einstein condensation*. Clarendon Press, Oxford (2003).
3. Barenghi, C.F., and Parker, N.G.: *A primer on quantum fluids*. Springer (2016).
4. Vinen, W.F.: The detection of single quanta of circulation in liquid helium II. *Proc. Roy. Soc. A* **260**, 218 (1961).
5. Hough, L., Donev, L.A.K., and Zieve, R.J.: Smooth vortex precession in superfluid  $^4\text{He}$ . *Phys. Rev. B* **65**, 024511 (2001).
6. Schwab, K., Bruckner, N., and Packard, R.E.: Detection of the Earth's rotation using superfluid phase coherence. *Nature* **386**, 585 (1997).
7. Pomeau, Y., and Rica, S.: Transition to dissipation in a model of superflow. *Phys. Rev. Lett.* **69**, 1644 (1992).
8. Keepfer, N.A., Stagg, G.W., Galantucci, L., Barenghi, C.F., and Parker, N.G.: Spin-up of a superfluid vortex lattice driven by rough boundaries. *Phys. Rev. B* **102**, 144520 (2020)
9. Comaron, P., Larcher, F., Dalfovo, F., and Proukakis, N.P.: Quench dynamics of an ultracold two-dimensional Bose gas. *Phys. Rev. A* **100**, 033618 (2019).
10. Donnelly, R.J., Donnelly, J.A., and Hills, R.N.: Specific heat and dispersion curve for helium II. *J. Low Temp. Phys.* **44**, 471 (1981).
11. Galli, D.E., Reatto, L., and Rossi, M.: Quantum Monte Carlo study of a vortex in superfluid  $^4\text{He}$  and search for a vortex state in the solid. *Phys. Rev. B* **89**, 224516 (2014).
12. Amelio, I., Galli, D.E., and Reatto, L.: Probing quantum turbulence in  $^4\text{He}$  by quantum evaporation measurements. *Phys. Rev. Lett.* **121**, 015302 (2018)
13. Berloff, N.G., and Roberts, P.H.: Motions in a Bose condensate: VI. Vortices in a nonlocal model. *J. Phys. A: Math Gen.* **32**, 5611 (1999).
14. Ortiz, G. and Ceperley, D.M.: Core structure of a vortex in superfluid  $^4\text{He}$ . *Phys. Rev. Lett.* **75**, 4642 (1995).
15. Sadd, M., Chester, G.V., and Reatto, L.: Structure of a vortex in superfluid  $^4\text{He}$ . *Phys. Rev. Lett.* **79**, 2490 (1997).
16. Barenghi, C.F., Vinen, W.F., and Donnelly, R.J.: Friction on quantized vortices in Helium II: a review. *J. Low Temp. Phys.* **52**, 189-247 (1982).
17. White, A., Proukakis, N.P., and Barenghi, C.F.: Non classical velocity statistics in a turbulent atomic Bose Einstein condensate. *Phys. Rev. Lett.* **104**, 075301 (2010).
18. Okamoto, N., Yoshimatsu, K., Schneider, K., Farge, M., and Kaneda, Y.: Coherent vortices in high resolution direct numerical simulation of homogeneous isotropic turbulence: a wavelet viewpoint. *Phys. Fluids* **19**, 115109 (2007).
19. Frisch, U.: *Turbulence. The legacy of A.N. Kolmogorov*, Cambridge University Press (1995).
20. Maurer, J., and Tabeling, P.: Local investigation of superfluid turbulence. *Europhys. Lett.* **43**, 29 (1998).
21. Salort, J., Chabaud, B., L ev eque, E., and Roche, P.-E.: Energy cascade and the four-fifths law in superfluid turbulence. *Europhys. Lett.* **97**, 34006 (2012).
22. Bradley, D.I., Fisher, S.N., Gu enault, A.M., Haley, R.P., Pickett, G.R., Potts, D., and Tsepelin, V. Direct measurement of the energy dissipated by quantum turbulence. *Nature Phys.* **7**, 473 (2011).
23. Nore, C., Abid, M., and Brachet, M.E.: Kolmogorov turbulence in low-temperature superflows. *Phys. Rev. Lett.* **78**, 3896 (1997).
24. Araki, T., Tsubota, M., and Nemirovskii, S.K.: Energy spectrum of superfluid turbulence with no normal-fluid component. *Phys. Rev. Lett.* **89**, 145301 (2002).
25. Kobayashi, M., and Tsubota, M.: Quantum turbulence in a trapped Bose-Einstein condensate. *Phys. Rev. A* **76**, 045603 (2007).
26. Baggaley, A.W., Barenghi, C.F., Shukurov, A., and Sergeev, Y.A.: Coherent vortex structures in quantum turbulence. *Europhys. Lett.* **98**, 26002 (2012).

27. Barenghi, C.F., L'vov, V., and Roche, P.-E.: Experimental, numerical and analytical velocity spectra in turbulent quantum fluid. *Proc. Nat. Acad. Sci. USA*, **111** (Suppl. 1) 4683 (2014).
28. Baggaley, A.W.: The importance of vortex bundles in quantum turbulence at absolute zero. *Phys. Fluids* **24**, 055109 (2012).
29. Andrew W. Baggaley, A.W., Laurie, J., and Barenghi, C.F.: Vortex-density fluctuations, energy spectra, and vortical regions in superfluid turbulence. *Phys. Rev. Lett.* **109**, 205304 (2012).
30. Roche, P.-E., and Barenghi, C.F.: Vortex spectrum in superfluid turbulence: interpretation of a recent experiment. *Europhys Lett.* **81**, 36002, (2008).
31. Paoletti, M.S., Fisher, M.E., Sreenivasan, K.R., and Lathrop, D.P.: Velocity statistics distinguish quantum turbulence from classical turbulence, *Phys. Rev. Lett.* **101**, 154501 (2008).
32. Vincent, A., and Meneguzzi, M.: The spatial structure and statistical properties of homogeneous turbulence. *J. Fluids Mech.* **225**, 1 (1991).
33. Baggaley, A.W., and Barenghi, C.F.: Quantum turbulent velocity statistics and quasiclassical limit. *Phys. Rev. E* **84**, 067301 (2011).
34. La Mantia, M., and Skrbek, L.: Quantum, or classical turbulence? *Europhys. Lett.* **102**, 46002, (2014).
35. Skrbek, L., Schmoranzner, D., Midlik, S., and Sreenivasan, K.R.: Phenomenology of quantum turbulence in superfluid helium. *Proc. Nat. Acad. Sci. USA* **118**, 16 (2021).
36. Farge, M., Pellegrino, G., and Schneider, K.: Coherent vortex extraction in 3D turbulent flows using orthogonal wavelets. *Phys. Rev. Lett.* **87**, 054501 (2001).
37. Volovik, G.E.: On developed superfluid turbulence. *J. Low Temp. Phys.* **136**, 309 (2004).
38. Walmsley, P.M., and Golov, A.I.: Quantum and quasiclassical types of superfluid turbulence. *Phys. Rev. Lett.* **100**, 245301 (1008).
39. Bradley, D.I., Clubb, D.O., Fisher, S.N., Guénault, A.M., Haley, R.P., Matthews, C.J., Pickett, G.R., Tsepelin, V., and Zaki, K.: Decay of pure quantum turbulence in superfluid  $^3\text{He-B}$ . *Phys. Rev. Lett.* **96**, 035301 (2006).
40. Baggaley, A.W., Barenghi, C.F., and Sergeev, Y.A.: Quasiclassical and ultraquantum decay of superfluid turbulence. *Phys. Rev. B* **85**, 060501(R) (2012).
41. Stagg, G.W., Parker, N.G., and Barenghi, C.F.: Ultraquantum turbulence in a quenched homogeneous Bose gas *Phys. Rev. A* **94**, 053632 (2016).
42. Cidrim, A., White, A.C., Allen, A.J., Bagnato, V.S., and Barenghi, C.F.: Vinen turbulence via the decay of multi-charged vortices in trapped Bose-Einstein condensates. *Phys. Rev. A* **96**, 023617 (2017).
43. Philip Mocz, P., Vogelsberger, M., Robles, V.H., Zavala, J., Boylan-Kolchin, M., Fialkov, A., and Hernquist, L.: Galaxy formation with BECDM – I. Turbulence and relaxation of idealized haloes. *M.N.R.A.S* **471**, 4559 (2017).
44. Barenghi, C.F., Sergeev, Y.A., and Baggaley, A.W.: Regimes of turbulence without an energy cascade. *Sci. Reports* **6**, 35701 (2016).
45. Barenghi, C.F., Hänninen, R., and Tsubota, M.: Anomalous translational velocity of vortex ring with finite-amplitude Kelvin waves. *Phys. Rev. E* **74**, 046303 (2006).
46. Vinen, W.F.: Decay of superfluid turbulence at a very low temperature: the radiation of sound from a Kelvin wave on a quantized vortex. *Phys. Rev. B* **64**, 134520 (2001).
47. Barenghi, C.F., Parker, N.G., Proukakis, N.P., and Adams, C.S.: Decay of quantised vorticity by sound emission. *J. Low Temp. Phys.* **138**, 629 (2005).
48. Svistunov, B.V.: Superfluid turbulence in the low-temperature limit. *Phys. Rev. B* **52**, 3647 (1995).
49. Leadbeater, M., Winiecki, T., Samuels, D.C., Barenghi, C.F., and Adams, C.S.: Sound emission due to superfluid vortex reconnections. *Phys. Rev. Lett.* **86**, 1410 (2001).
50. Zuccher, S., Caliari, M., Baggaley, A.W., and Barenghi, C.F.: Quantum vortex reconnections, *Phys. Fluids* **24**, 125108 (2012).
51. Galantucci, L., Baggaley, A.W., Parker, N.G., and Barenghi, C.F.: Crossover from interaction to driven regimes in quantum vortex reconnections. *Proc. Nat. Acad. Sci. USA* **116**, 12204 (2019).
52. Morishita, M., Kuroda, T., Sawada, A., and Satoh, T.: Mean free path effects in superfluid  $^4\text{He}$ . *J. Low Temp. Phys.* **76**, 387 (1989).

53. Schwarz, K.W.: Three-dimensional vortex dynamics in superfluid  $^4\text{He}$ : homogeneous isotropic turbulence. *Phys. Rev. B* **38**, 2398 (1988).
54. Kida, S.: A vortex filament moving without change of form. *J. Fluid Mech.* **112**, 397 (1985).
55. Ricca, R.L., Samuels, D.C., and Barenghi, C.F.: Evolution of vortex knots. *J. Fluid Mech.* **391**, 29 (1999).
56. Proment, D., Onorato, M., and Barenghi, C.F.: Vortex knots in a Bose-Einstein condensate. *Phys. Rev. E* **85**, 036306 (2012).
57. Oberti, C., and Ricca, R.L.: Influence of winding number on vortex knots dynamics. *Sci. Reports* **9**, 1 (2019).
58. Kleckner, D., Kauffman, L.H., and Irvine, W.T.M.: How superfluid vortex knots untie, *Nat. Phys.* **12**, 650 (2016).
59. Liu, X. and Ricca, R.L.: Knots cascade detected by a monotonically decreasing sequence of values. *Sci. Rep.* **6**, 24118 (2016).
60. Xin Liu, X., Ricca, R.L., and Li, X.-F.: Minimal unlinking pathways as geodesics in knot polynomial space. *Comm. Phys.* **3**, 1 (2020)
61. Kleckner, D. and Irvine, W.T.M.: Creation and dynamics of knotted vortices. *Nat. Phys.* **9**, 253 (2013).
62. Mesgarnzhad, M., Cooper, R.G., Baggaley, A.W., and Barenghi, C.F.: Helicity and topology of a small region of quantum vorticity. *Fluid Dyn. Res.* **50**, 011403 (2018).
63. Cooper, R.G., Mesgarnzhad, M., Baggaley, A.W., and Barenghi, C.F.: Knot spectrum of turbulence. *Sci. Reports* **9**, 10545 (2019)
64. Barenghi, C.F., Ricca, R.L., and Samuels, D.C.: How tangled is a tangle? *Physica D* **157**, 197 (2001).
65. Moffatt, H.K.: Degree of knottedness of tangled vortex line, *J. Fluid Mech.* **35**, 117 (1969).
66. Clark di Leoni, P., Mininni, P.D., and Brachet, M.E.: Dual cascade and dissipation mechanisms in helical quantum turbulence. *Phys. Rev. A* **95**, 053636 (2017).
67. Moffatt, H.K., and Ricca, R.L.: Helicity and the Călugăreanu invariant, *Proc. Roy. Soc. London A* **439**, 411 (1992).
68. Hänninen, R., Hietala, N., and Salman, H.: Helicity within the vortex filament model. *Sci. Reports* **6**, 37571 (2016).
69. Zuccher, S. and Ricca, R.L.: Twist effects in quantum vortices and phase defects. *Fluid Dyn. Res.* **50**, 011414 (2018).
70. Salman, H.: Helicity conservation and twisted Seifert surfaces for superfluid vortices. *Proc. Roy. Soc. A* **473**, 20160853 (2018)
71. Galantucci, L., Barenghi, C.F., Parker, N.G., and Baggaley, A.W.: Mesoscale helicity distinguishes Vinen from Kolmogorov turbulence in helium-II. *Phys. Rev. B* **103**, 144503 (2021).
72. Livingstone, L.: *Knot Theory* Cambridge University Press, Cambridge (1993).
73. Arsuaga, J., Vasquez, M., Trigueros, S., Summers, D.W., and Roca, J.: Knotting probability of DNA molecules confined in restricted volumes: DNA knotting in phage capsids. *Proc. Nat. Acad. Sci. USA* **99**, 5373 (2002).
74. Raymer, D.M. and Smith, M.: Spontaneous knotting of an agitated string. *Proc. Nat. Sci. Acad. Sci. USA* **104**, 16432 (2007).